



1595 Norway Street, Town of Mount Royal
Quebec, Canada, H4P 1Y3
Phone: 001-514-342-2982
E-mail: ion.paraschivoiu@polymtl.ca
www.iopara.ca

MODELING BLADE PITCH AND SOLIDITIES IN STRAIGHT BLADED VAWTS

FINAL REPORT

Under the request of

Wind Harvest International Inc.
11431 Highway One, Suite 12
P.O. Box 358
Point Reyes Station, CA 94956-0358

Montreal
August 2nd, 2011

TABLE OF CONTENTS

1. INTRODUCTION.....	3
2. IMPLEMENTATION OF THE AERODYNAMIC FORCES AND MOMENTS CALCULATION (TASK 1.2).....	4
3. IMPLEMENTATION OF THE GENETIC-ALGORITHM BASED OPTIMIZATION AND VARIABLE PITCH ANGLE (TASK 1.4).....	4
4. SOLIDITY PARAMETRIC STUDY (TASK 2.1).....	7
4.1 GEOMETRIC PARAMETERS.....	7
4.2 CONTROL PARAMETERS.....	8
4.3 OPERATIONAL PARAMETERS.....	9
4.4 SOLIDITY ANALYSIS RESULTS.....	9
5. EVALUATION OF THE DRAG IN THE WHI 1500 AND EXTENDED WHI 1500 MODELS (TASKS 3.1 AND 3.2).....	12
5.1 LENTICULAR FAIRING DRAG COEFFICIENTS CALCULATION.....	12
5.2 BLADE ARM DRAG CALCULATION.....	20
6. EVALUATION OF THE CHANGES TO FAIRING AND BLADE END DESIGN (TASK 3.3)	25
7. SIMULATION OF AN ARRAY OF 3 VAWT WITH DIFFERENT PLACEMENT OF COLUMNS (TASK 3.4).....	26
7.1 CASE 1 - COLUMNS ARE PLACED IN BETWEEN ROTORS.....	27
7.2 CASE 2 - COLUMNS ARE PLACED IN FRONT OF ROTORS.....	31
7.3 DISCUSSION ON CASE 1 VS. CASE 2.....	35
8. EFFECT OF WIND DIRECTION ON ROTOR PERFORMANCE (TASK 3.5).....	37
8.1 CASE 1 - CO-ROTATING ROTORS.....	40
8.2 CASE 2 - COUNTER-ROTATING ROTORS (WHI 3000).....	47
9. SPACING STUDY FOR MULTIPLE WHI 3000 TURBINES (TASK 3.5).....	52
9.1 PROBLEM DESCRIPTION.....	52
9.2 ANALYSIS AT TSR = 2.....	54
9.3 ANALYSIS OF DIFFERENT ROTATION SPEED OF THE TOP AND BOTTOM ROTORS.....	56
9.4 ANALYSIS FOR TSR = 3.....	57
10. TORQUE LIMITING PITCH ANALYSIS (TASKS 4.1, 4.2 AND 4.3).....	59
10.1 OBJECTIVES.....	59
10.2 METHODOLOGY.....	59
10.3 TORQUE LIMITING PITCH RESULTS.....	59
11. CONCLUSIONS AND RECOMMENDATIONS.....	64
APPENDIX 1.....	66
REFERENCES.....	68

1. INTRODUCTION

This report is a compilation of the aerodynamic analyses carried out by IOPARA Inc. as part of a contract project called "Modeling Blade Pitch and Solidities in Straight Bladed VAWTs," realized under the request of Wind Harvest International Inc. (WHI). The tasks undertaken during this project are:

1. Prepare the computer programs to compute the pitch angle parametric results.
 - 1.2 Prepare the program to compute the aerodynamic forces and moments of the pitching blades.
 - 1.4 Implement a variable pitch angle methodology in the model.
2. Conduct the solidity parametric study to determine performances of coupled vortex augmented rotors having the specified solidities.
 - 2.1 Calculated C_p vs. TSR for different solidities.
 - 2.2 Use computer model to calculate energy output.
 - 2.3 Perform LCOE analysis.
3. Use CARDAAV to determine an improved low drag design.
 - 3.1 Evaluate drag in the model 1500 design.
 - 3.2 Evaluate the same drag in extended model 1500 design.
 - 3.3 Evaluate changes to fairing and blade end design.
 - 3.4 Evaluate the effects of the frame on turbine performance.
 - 3.5 Determine the relationship between turbine aerodynamic performance, wind direction and rotor spacing.
4. Determine the optimum pitch angles to limit torque of the best solidity rotor.
 - 4.1 Compute blade aerodynamic forces and moments at pitch angles and wind speed increments.
 - 4.2 Calibration and validation of genetic-algorithm based optimization.
 - 4.3 Perform blade pitch parametric optimization studies.

In the sections that follow, details of the work realized on the tasks outlined above are discussed. The report ends with some brief conclusions and recommendations based on the completed analyses.

2. IMPLEMENTATION OF THE AERODYNAMIC FORCES AND MOMENTS CALCULATION (TASK 1.2)

The CARDAAV code is based on the Double-Multiple Streamtube model with variable upwind and downwind induced velocities in each streamtube (DMSV) [1]. By applying in each streamtube the momentum equation to the control volumes that contain the actuator disks, the forces on the disks can be determined. The forces on the disks are calculated by using the blade element theory, which involves the aerodynamic lift and coefficients of the blade airfoil.

Thus, with the CARDAAV code it is possible to extract the aerodynamic loads applied on the blades, i.e. the normal and tangential forces applied along the length of the blade and for different azimuthal positions. These aerodynamic loads are calculated at the aerodynamic center of the blade airfoil and if one knows the location of the pitching blade hinge, the resultant forces (at the blade hinge) can be calculated. Moreover, if the mass and center of mass of the blade are known, the centrifugal force can also be taken into account in the resultant forces calculation for all azimuthal positions of the blade.

3. IMPLEMENTATION OF THE GENETIC-ALGORITHM BASED OPTIMIZATION AND VARIABLE PITCH ANGLE (TASK 1.4)

To search for the best pitch schedule to limit torque as wind speeds reach generation capacity, an optimization procedure [2, 3] for best pitch to limit torque was adopted that made use of a genetic algorithm (GA) based optimization technique [4]. In this optimization technique (see Figure 1), an initial "population" composed of "individuals," which are solutions of the analyzed problem (which in this case is the performance analysis of the VAWT) at some particular, randomly selected, values of the optimization variables (which is in this case are variables that define the pitch angle schedule), is first generated.

The next generation or population is then obtained on the principle of the survival of the fittest. However, 3 intermediate operations are typically performed by the genetic algorithms on the analyzed "population." These operations are: (1) "selection" (choice of the "individuals" for the next generation, according to a "survival of the fittest" criterion), (2) "crossover" (operation which allows information exchange between the "individuals" by swapping parts of the parameter vector in an attempt to get better "individuals"), and (3) "mutation" (operation which introduces new or prematurely lost information in the form of random changes applied to randomly chosen vector components).

Like in any optimization study, an "objective function" had to be defined that is either to be minimized or maximized. In this study, objective is to limit the inverse of the rotor power, for given conditions of operation (wind speed, rotational speed). Thus, the objective function can be written as:

$$F_{\min} = f(T_{\max \text{ allowable}}, T_{\text{calc}}) \quad (1)$$

Since for a Vertical Axis Wind turbine (VAWT), the local angle of attack α of a blade element:

$$\alpha = \sin^{-1} \left[\frac{\cos \theta \cos \tau - (X - \sin \theta) \sin \tau}{\sqrt{(X - \sin \theta)^2 + \cos^2 \theta}} \right] \quad (2)$$

Contains the blade pitch angle τ , the later influences the aerodynamic characteristics, the torque and ultimately the power output of the rotor. Since it is desirable to have a smooth variation [5] of the pitch angle during a complete rotation of the turbine blade, the following analytical expression was considered for the blade pitch angle τ with the azimuth angle θ :

$$\tau = x_1 \cos \theta + x_2 (\sin \theta)^{x_3} \quad (3)$$

The optimization procedure is then used to obtain optimum values of the variables x_1 , x_2 and x_3 , such that the resulting pitch angle schedule minimizes the objective function F or maximizes the turbine power P . Hence, through relations (2) and (3) an indirect link is established between the objective function (1) and the optimization variables x_1 , x_2 and x_3 , which control the variation of τ .

The genetic algorithm evolution strategy optimization package, GENIAL v1.1 [4] was employed to minimize the objective function. This code includes 3 main modules, which perform the above mentioned operations. A number of parameters are available in each module to control its functioning during the optimum search process. As mentioned above, the coefficients x_1 , x_2 and x_3 of the pitch variation function (3) were used as optimization variables. Their values were subjected to certain constraints, to avoid any possible mathematical invalidity and to keep the pitch angle within reasonable or practical (technically feasible) limits.

As a first step, an optimization tool [3] was developed that included both GENIAL and CARDAAV (in-house analysis code for VAWTs). Figure 1 shows a flow chart of the optimization methodology. The program first reads the input parameters that control the optimization process, namely those that are frequently changed (size of the "population" – number of "individuals", number of evaluations, constraints to be set on the optimization variables). For each combination of the optimization variables, defining a distinct "individual", GENIAL calls (using a "system function") PITCH, then CARDAAV, which performs the analysis of the VAWT for that specific variation of the blades' pitch angle. With the turbine power, calculated by CARDAAV, the objective function (1) is determined and based on it, the "fitness function" which characterizes that "individual" is obtained. Depending on its "fitness" an "individual" can be maintained or eliminated from the "population" during the optimization process.

Selection, crossover and mutation are used to advance the "population" from 1 optimization cycle to the next until the optimum or the predefined limit of evolutions is reached. At the end of the optimization, MAIN outputs the optimal values of the x_1 , x_2 and x_3 variables (as found through optimization), which define the best variation law for the pitch angle. Corresponding to this, the performance characteristics of the turbine are computed and stored in a file for post-processing purposes.

As the name indicates, the subroutine PITCH uses relation (3) to calculate the pitch angle over the entire circular trajectory of the blades, based on the values of x_1 , x_2 and x_3 received from GENIAL. It stores the azimuthal and the pitch angles in a file where CARDAAV seeks this information before performing each new analysis.

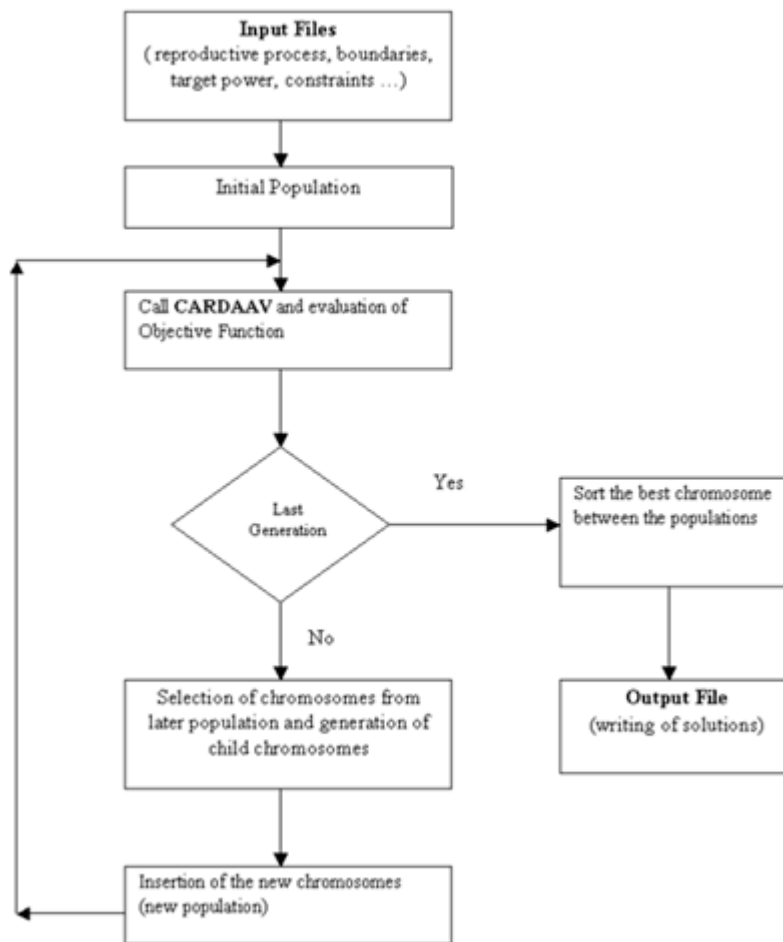


Figure 1: Flow chart showing the GA based optimization procedure [6].

Further details of the GA based optimization procedure and the coupling of GENIAL and CARDAAV can be found in [6].

4. SOLIDITY PARAMETRIC STUDY (TASK 2.1)

Different rotor solidities ranging from 12.375 % to 33 % were evaluated as part of the solidity parametric analysis, in order to determine the effect of the rotor solidity on the performance of coupled vortex augmented rotors. The rotor solidities were calculated using equation 4:

$$Solidity = \frac{Nc}{2R} \quad (4)$$

Where: N is the number of blades
 c is the blade chord length
 R is the rotor radius

The C_p vs. TSR for a rotor solidity of 16.5 % was calculated using the dimensions of the WHI 3000 provided by WHI during a previous project called "Aerodynamic Model of the Wind Harvest International 3000 Wind Turbine" [7]. The C_p vs. TSR for the rotor solidity of 33 % was calculated for a 6-bladed model 1500 turbine in a previous project called "Aerodynamic Model of the Wind Harvest International 1500 Wind Turbine" [8]. Furthermore, a rotor solidity of 12.375 % and 24.75 % were calculated during this project and included in this analysis.

4.1 Geometric Parameters

The rotor dimensions used for the solidity parametric analysis are presented in Table 1 and were based on the WHI 3000 dimensions provided during the previous project [7].

Table 1: Dimensions of the WHI 3000

Rotor height	11.83 m (38.8 ft)
Rotor diameter	Variable
Number of blade per rotor	4
Blade shape	Straight blade
Blade airfoil	NACA0018
Blade chord length	0.9750 m (38.387 in)
Number of blade arms per blade	2
Blade arm airfoil	NACA0021
Blade arm positions	At the extremities of the blades
Blade arm chord length	Outer section: 0.3317 m (13.06 in) Inner section: 0.4267 m (16.8 in)
Blade arm thickness	Outer section: 0.0889 m (3.5 in) Inner section: 0.1143 m (4.5 in)
Blade arm length	Outer section: variable Inner section: 6.0960 m (240 in)
Central shaft diameter	0.219 m (8.625 in)
Number of support cables per blade	2
Support cable diameter	0.01905 m (0.75 in)

For the attachment points of the support cables, it was considered that they are extending from the upper blade arm junction with the central shaft to the lower blade arm (240 inches and 30 inches radially in from the blade). Also, the power loss related to the parasitic drag of the support cables was considered, but not the associated flow perturbation on the downstream half of the rotor. Moreover, the blade arm geometry of the WHI 3000 is lenticular in shape (as depicted in Figure 2) with a thickness-to-chord (t/c) ratio of 0.2679. Because of this large ratio, the aerodynamic properties of a NACA0021 profile were used in CARDAAV (for this analysis), but with the dimensions of the actual blade arm. Furthermore, the presence of the frame was not considered.

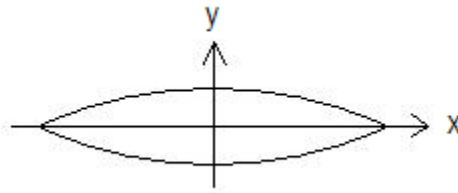


Figure 2: WHI 3000 blade arm cross-section.

For the rotor solidity of 33 %, only 1 support cable was considered, connecting to the lower blade arm 30 inches radially in from the blade. Also, the dimensions of the outer section (blade arm chord length and thickness) were used for the entire length of the blade arm, composed of only 1 section. Moreover, the performance calculation of the rotor solidity of 33 % included the correction factors for high solidity calibrated for the 6-bladed WHI 1500 [8] (rotor solidity of 33 %) and was not validated by CFD calculations in the case of the 4-bladed version.

4.2 Control Parameters

The following inputs were used as control parameters for this analysis:

1. Analysis in a horizontal laminar wind (wind skew angle = 0° , turbulence level = 0 %).
2. Power law atmospheric wind shear exponent of 0.16 (i.e. level country with foot-high grass and occasional tree [9]).
3. Wind speed reference height at the equatorial height of the rotor.
4. Taking into account the effect of dynamic stall by using the Gormont-Berg model.
5. Taking into account the corrections for the secondary effects related to the:
 - Finite span of the blades
 - Wake of the rotating central shaft
 - Parasitic drag of the struts
 - Parasitic drag of the support cables
6. Air properties corresponding to dry air at standard atmosphere (101.325 kPa) and a temperature of 15 8C:
 - Air density : 1.225012 kg/m³
 - Air kinematic viscosity: 1.486895E-05 m²/s

4.3 Operational Parameters

The aerodynamic performances of the turbines were evaluated for a wind speed range of 10.07 mph to 64.87 mph (when convergence was obtained).

4.4 Solidity Analysis Results

Using the input parameters described in sections 4.1 to 4.3, the aerodynamic performances of the WHI 3000 with coupled vortex effect was calculated using CARDAAV for different rotor solidities: 12.375 %, 16.5 % and 24.75 % and 33 %.

The variation in rotor solidities was obtained by modifying the rotor radius through a change in the length of the outer blade arms. Hence, the length of the inner blade arm, blade chord and the position of the attachment points of the support cables on the lower blade arm remained at their original values.

Concerning the operational characteristics, in order to maintain the same centrifugal force in the blades for all rotor solidities, the rotational speed of the rotors were modified depending on the rotor radius and the blades' centrifugal force of the WHI 3000 with a rotor solidity of 16.5 % was used as the reference value. Table 2 presents the values of the variable geometric parameters and rotational speeds associated with each rotor solidity.

Table 2: Geometric and operational characteristics for different rotor solidities

Rotor solidity (%)	Rotor radius (m)	Swept area (m²)	Rotational speed (rpm)
12.375	15.76	372.82	25.24
16.50	11.82	279.62	29.15
24.75	7.88	186.41	35.70
33.00	5.91	139.81	41.22

Recent CFD analysis of the WHI 3000 in a close proximity linear array (Figure 3) showed that the coupled vortex effect influences the torque generated by the blades on the upstream and downstream half of the rotor.

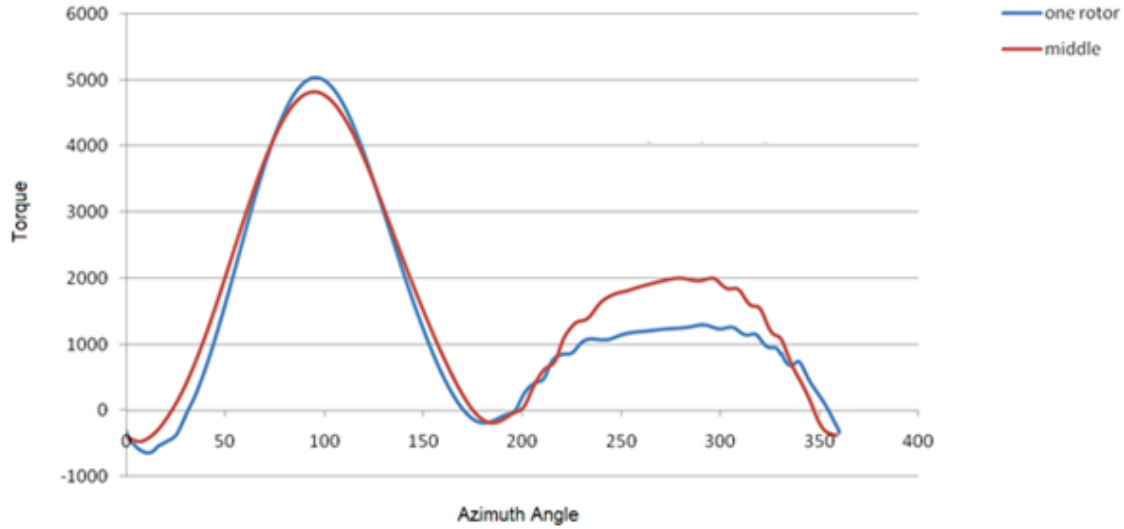


Figure 3: Comparison of torque on 1 blade for a single rotor and an array of 3 rotors for the WHI 3000.

Based on this result, 2 amplification factors were considered in order to account for the effects on performance related to the coupled vortex effect, 1 for the upstream velocity distribution (reaching the upstream half of the rotor) and 1 for the downstream velocity distribution (reaching the downstream half of the rotor). The amplification factors were applied on the velocities in the form of a 2nd degree polynomial (i.e. a parabolic distribution). A concave distribution was used for the upstream velocities (Figure 4a) and a convex distribution was used for the downstream velocities (Figure 4b).



Figure 4: Parabolic distribution of the amplification factors: a) on the upstream half of the rotor; b) on the downstream half of the rotor.

The amplification factors for the WHI 3000 were calibrated based on the fine mesh CFD results and a linear amplification factor corresponding to equation 5 was applied on the upstream velocities and a fixed amplification factor of 1.05 was applied on the downstream velocities.

As we may see from Figure 5, those amplification factors provide a good agreement between the CARDAAV and CFD results for the rotor solidity of 16.5 %. However, one should mention that those amplification factors were also used for the other analyzed rotor solidities and additional CFD computations would be required to calibrate the amplification factors for those other solidities.

$$f_{\text{amplification}} = 0.1 \cdot (V_{\infty} + 1.65), \text{ where } V_{\infty} \text{ is in m/s} \quad (5)$$

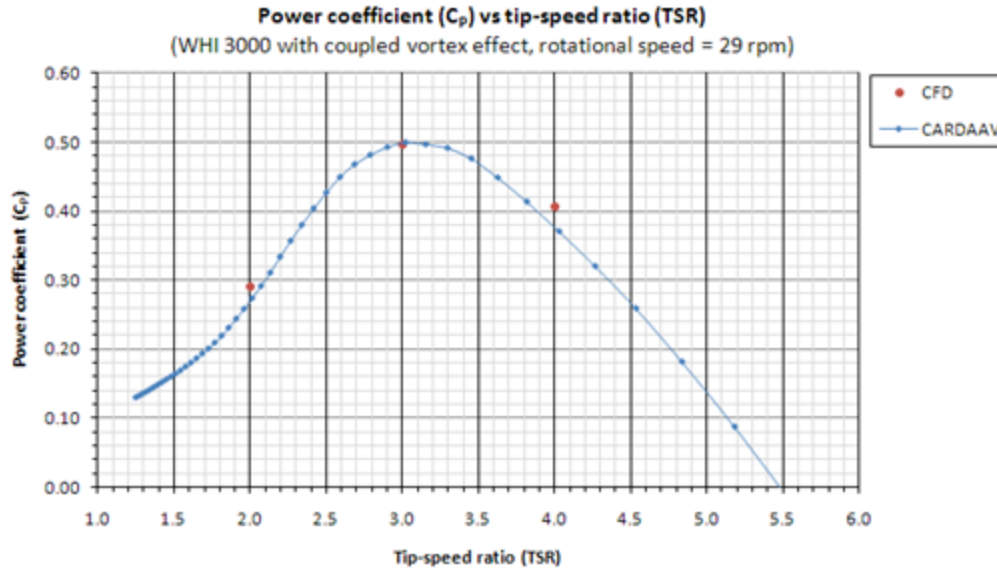


Figure 5: Power coefficient (C_p) vs. tip-speed ratio (TSR). Comparison between CFD and CARDAAV results.

Table 3 and Figure 6 present the results of the solidity parametric analysis. Also, one should mention that the results presented in this report relate to the mechanical power. The actual amount of electrical power generated by the wind turbine will be lower by a factor that depends on the efficiency of the major components which are involved in the mechanical-to-electrical power conversion.

Table 3: Maximum power coefficient and associated tip-speed ratio and wind speed for different rotor solidities with coupled vortex effect of counter rotating turbines

Rotor solidity (%)	Max. power coefficient (%)	TSR	Wind speed (mph)
12.375	47.50	3.47	26.84
16.50	49.38	3.01	26.84
24.75	47.27	2.45	26.84
33.00	31.95	1.96	29.08

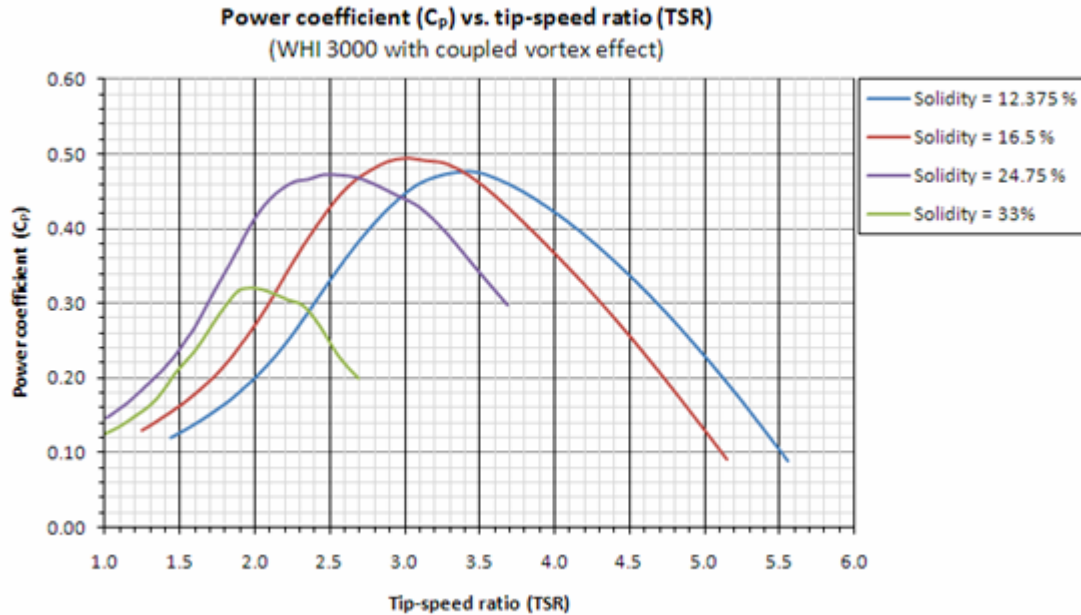


Figure 6: Power coefficient (C_p) vs. tip-speed ratio (TSR) for different rotor solidities.

As we may see from Table 3 and Figure 6, the maximum power coefficient is obtained for a rotor solidity of 16.5 % ($C_p = 49.38$ % at $TSR = 3.01$).

5. EVALUATION OF THE DRAG IN THE WHI 1500 AND EXTENDED WHI 1500 MODELS (TASKS 3.1 AND 3.2)

5.1 Lenticular Fairing Drag Coefficients Calculation

The objective of this task is to evaluate the drag losses in the WHI 1500 and WHI 3000 model (extended WHI 1500), caused by fairings. Drag is due to both pressure and viscous forces, the latter being the most important cause of drag.

Flow past the fairing profile presents the same aerodynamic features as airfoils and poses the same challenges for analysis. At relatively low Reynolds numbers (Re), flow in the boundary layer of an airfoil is neither completely laminar nor completely turbulent, thus a transition occurs from laminar to turbulent. This is a challenge for CFD simulations since numerical models have difficulty modeling transition. The CFD specifications for the drag calculations are presented in Figure 7.

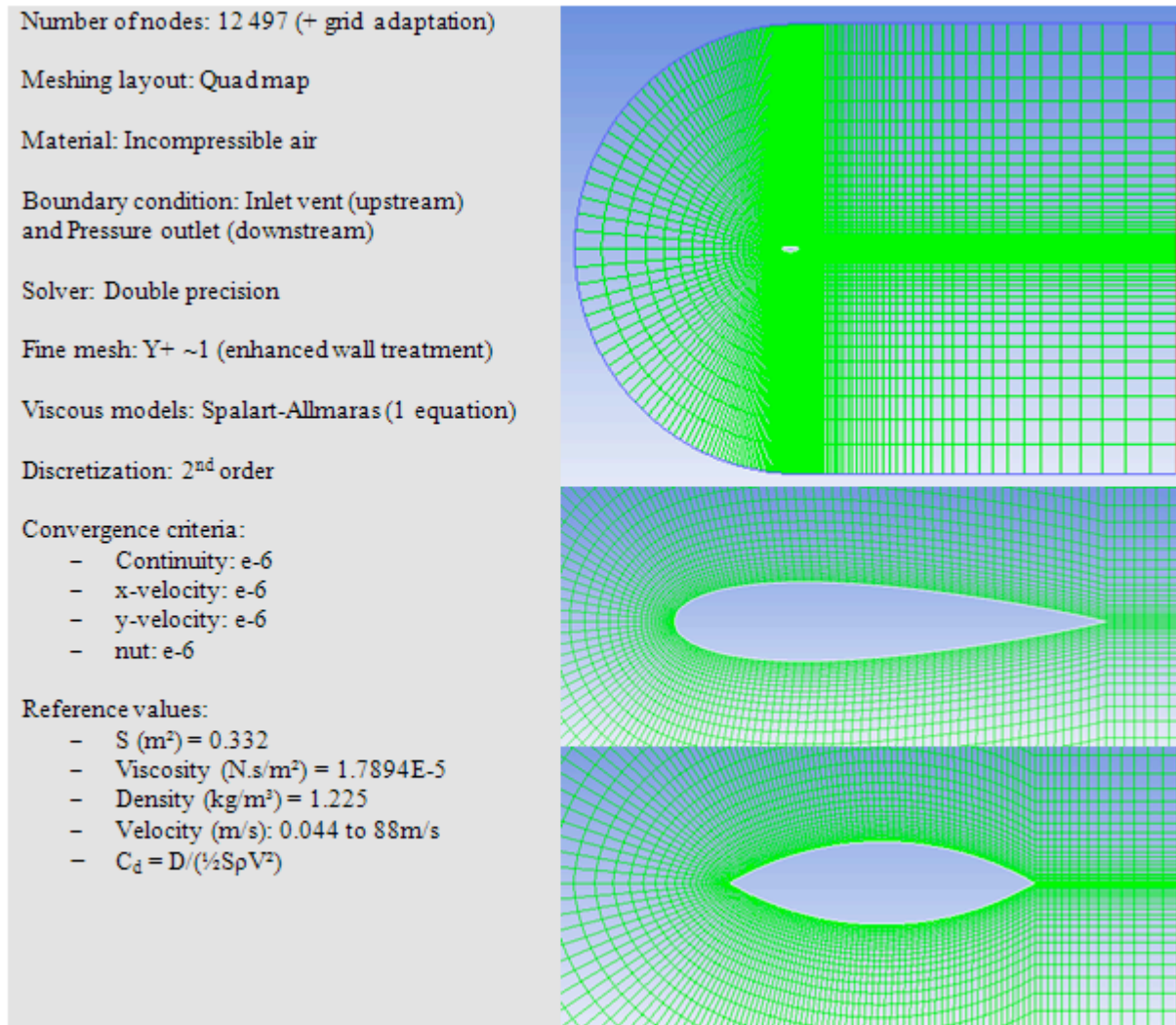


Figure 7: CFD parameters.

The drag coefficients for the lenticular fairing were evaluated for a range of Reynolds numbers using CFD using the following method:

1. For purpose of validation and calibration, a CFD model was designed for a reference airfoil, the NACA0018 and the drag coefficients were computed for a range of Reynolds number relevant to the operating range of the WHI turbines. The results were compared with experimental data from Sandia National Laboratories [10]. Different viscous models were tested and the numerical model was adjusted to achieve the best accuracy.

The laminar viscous model only works for fully laminar flows, which is not the case here. Transition models designed for transition flow, such as “Transition k-kl- ω ”, work well starting from intermediate Re ($10E6$), but not for very low Re ($1000 - 160,000$) which we need in our case. The Spalart-Allmaras (S-A) model, which is often use for wind turbines and airfoils, works well for all Re , but is designed for turbulent flow as it considers the whole boundary layer as turbulent, thus it would overestimates drag in transition flow.

Further to our experiments, we concluded that the most accurate method for evaluating the drag of the lenticular fairings, in the given low Re range, is to use the Spalart-Allmaras viscous model with a constant correction factor in order to offset the error caused by considering the whole boundary layer turbulent. See details in APPENDIX 1.

With the reference values presented in Figure 7 and a chord length of 0.332 m ($13^{1/4}$ in), the given Reynolds numbers cover a velocity range from 0.044 to 88 m/s, which fits the relative velocities on the fairings at different TSR values.

The present fairing profile has a relative thickness (e) of 26.79 %, with a maximum thickness at $c/2$ (50 % of the chord length). The geometric parameters of the tested fairings are presented in Figure 8.

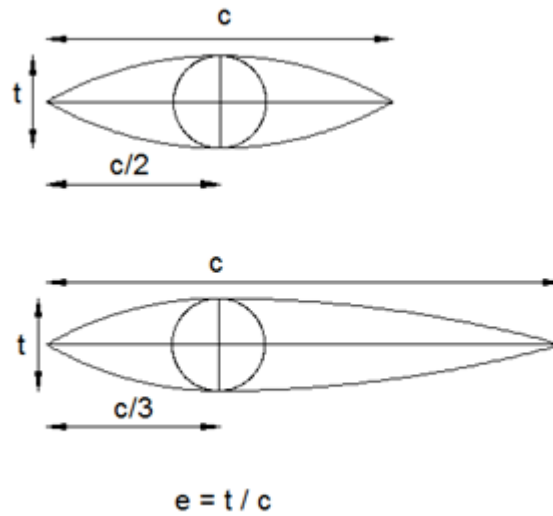


Figure 8: Fairing profiles geometries.

2. Once the CFD model was adjusted, the same layout and settings were used for the lenticular fairing. Again, the C_d was computed for a relevant range of Reynolds number and the results were compared to the CFD results of the NACA0018, in order to evaluate the aerodynamic performance of this profile in comparison with a reference airfoil.

The following figures summarize the results of these simulations.

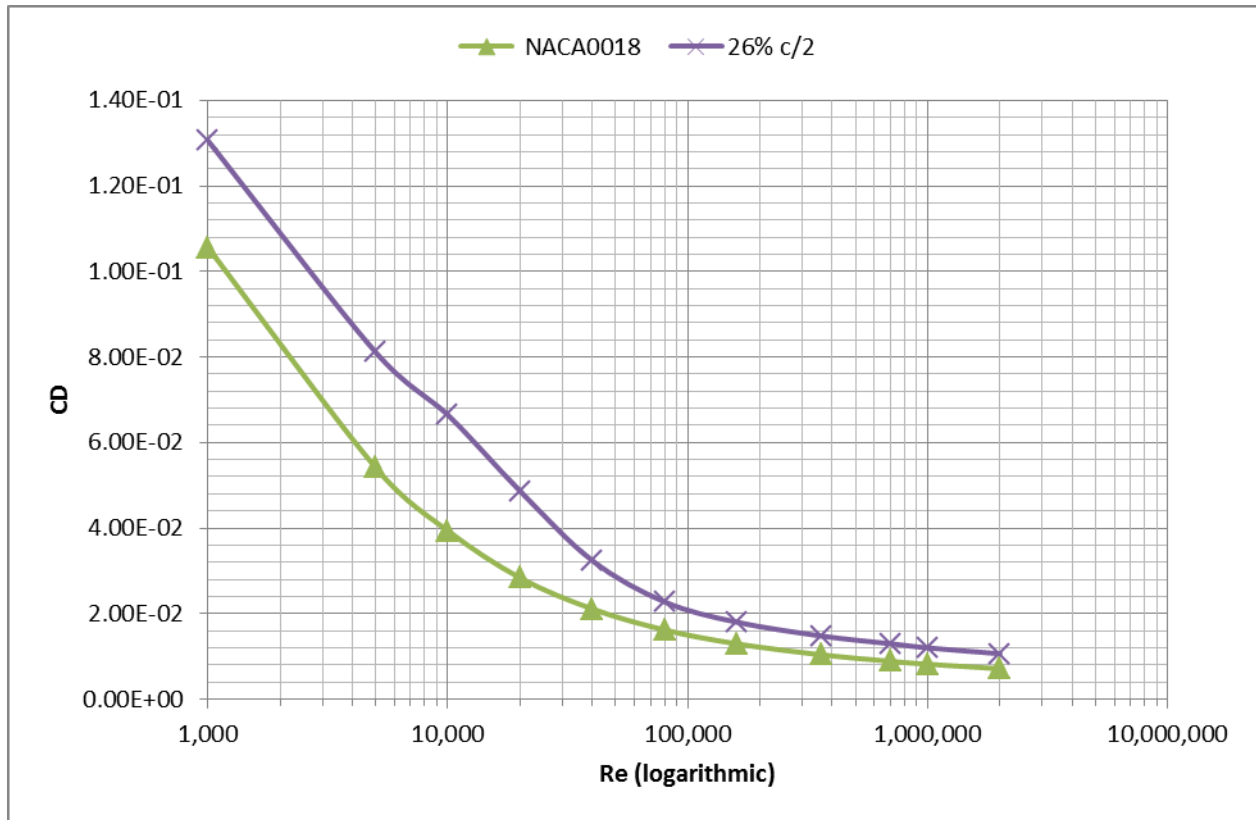


Figure 9: NACA0018 compared to WHI drag coefficient (C_d) vs. Reynolds number (Re) (logarithmic scale), CFD values with correction factor.

We can see in Figure 9 that the drag coefficients of the WHI fairing ($t/c = 26.8\%$ at $c/2$) are substantially higher than the NACA0018, about 48% higher in average. This variation is mainly due to the higher relative thickness that causes separation by increasing pressure gradients.

3. In order to assess the influence of relative thickness, we simulated a modified lenticular shape with a relative thickness of 18%, which is the relative thickness of a NACA0018. The maximum thickness in this case is at $c/2$ as the current WHI fairing shape. The drag coefficients of the modified design were computed and the results were compared with the reference airfoil. Figure 10 presents the results of this simulation.

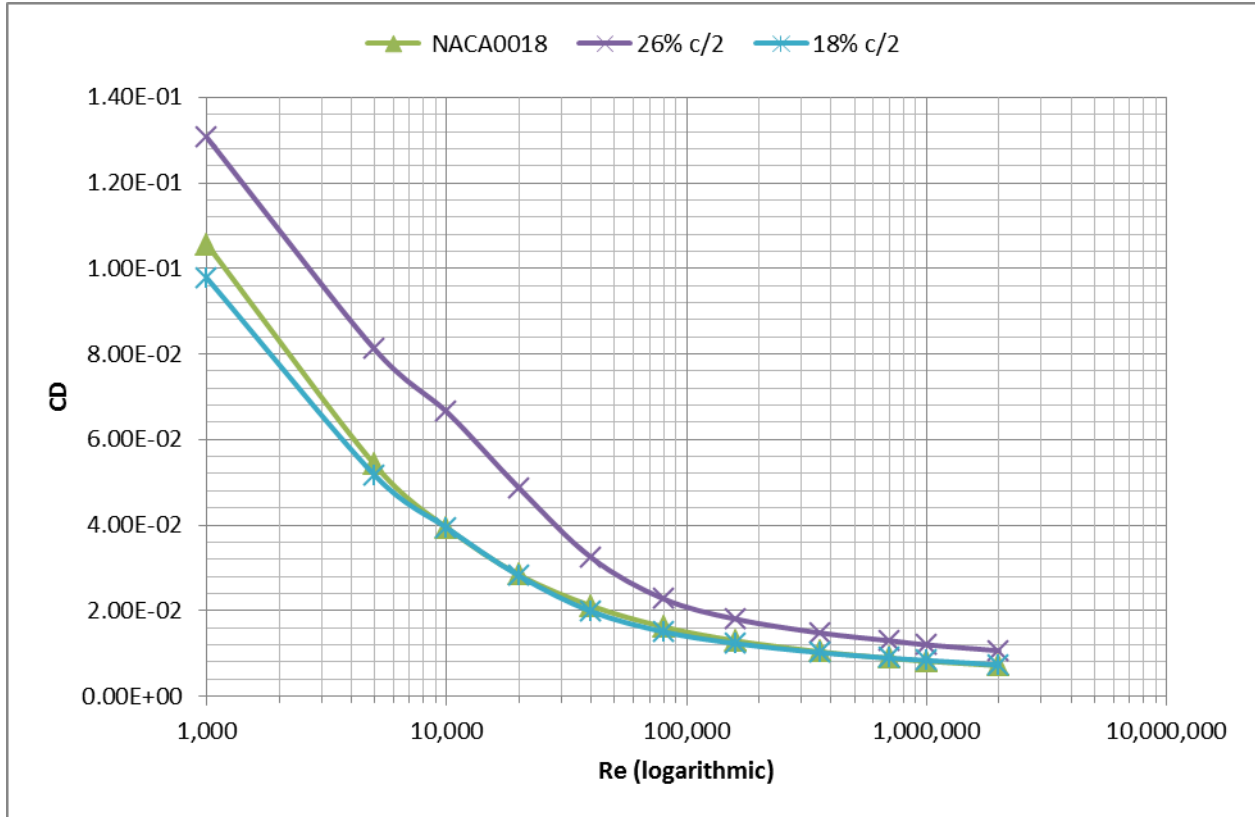


Figure 10: WHI 18 % $c/2$, NACA0018, WHI 26.79 % $c/2$, drag coefficient (C_d) vs. Reynolds number (Re (logarithmic scale), CFD values with correction factor.

We can see in Figure 10 that the lenticular profile with 18 % relative thickness at $c/2$ has a C_d very similar to NACA0018. Its C_d is actually 2 % lower in average.

- Following the previous experiment, in order to assess the influence of maximum the thickness point, we simulated a modified lenticular shape with a relative thickness of 18 %, with the maximum thickness at $c/3$ similarly to a NACA airfoil. The drag coefficients of the modified design were computed and the results were compared with the reference airfoil. Figure 11 presents the results of these simulations.

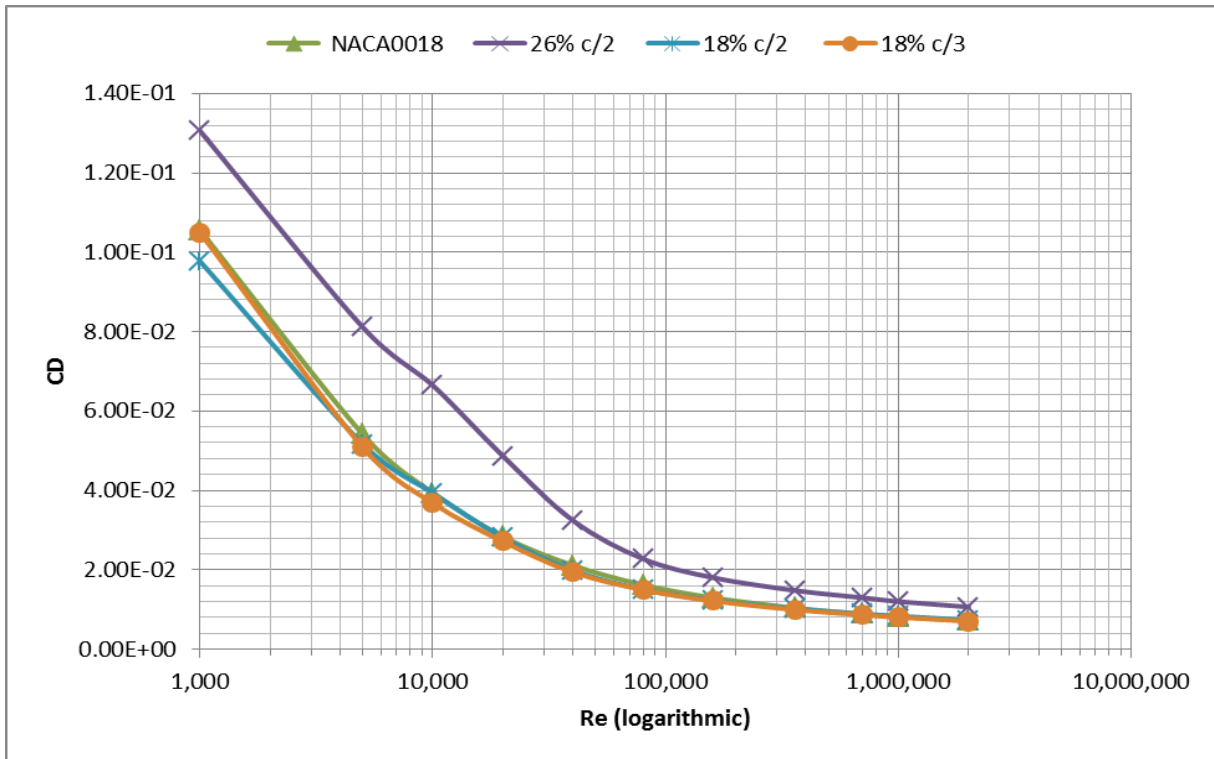


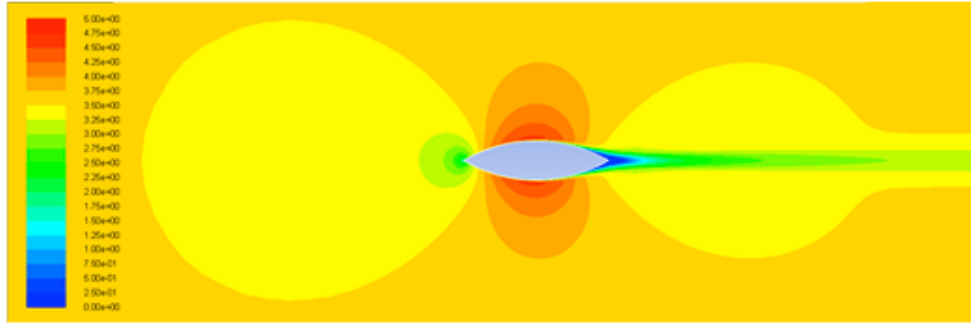
Figure 11: WHI 18 % $c/3$, NACA0018, WHI 26.79 % $c/2$, WHI 18 % $c/2$, drag coefficient (C_d) vs. Reynolds number (Re) (logarithmic scale), CFD values with correction factor.

We can see in Figure 11 that the lenticular profile with 18 % relative thickness at $c/3$ has a C_d very close to NACA0018. Its C_d is actually 3 % lower in average.

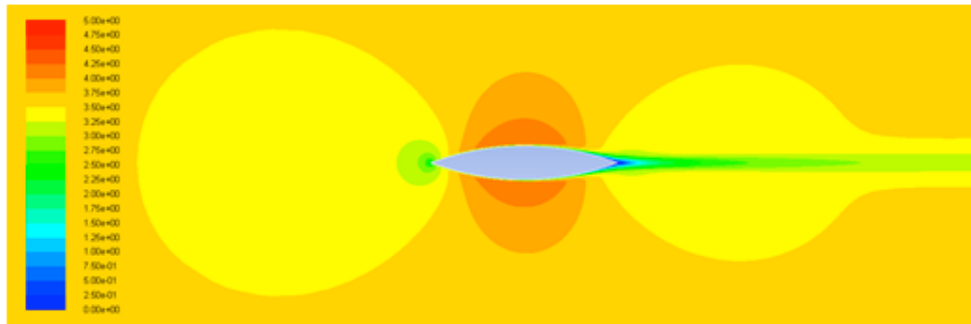
In Figure 12, we can observe the velocity distribution along the different tested profiles. The blue color refers to zero velocity. In Figure 12a, corresponding to WHI current fairing profile (26.79 %, $c/2$), the wake is stronger since the flow is slowed down more, as it is illustrated by the significant blues area around the trailing edge. Figure 12b displays the modified lenticular profile (18 %, $c/2$). We can clearly observe the reduction in the wake with a smaller blue area; the reduction is even more evident in Figure 12c referring to the second modified profile (18 %, $c/3$).

Strong pressure gradients will cause the flow to detach. A smaller relative thickness causes smaller pressure gradients and thus reduces separation. Moreover, if the maximum thickness is located closer to the nose of the profile, then for similar chord length, the flow has more length to reattach. This is why the 18 % at $c/3$ profile gives better results, although the variation between profiles of equal relative thickness is very small, as seen in Figure 11.

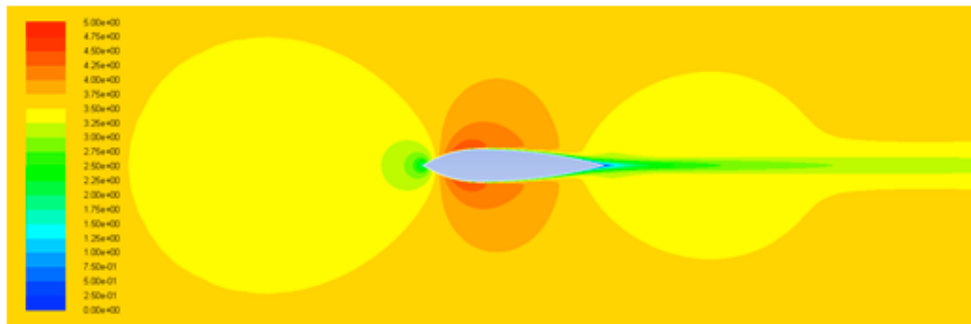
The flow for 18 % at $c/2$ is very similar to the NACA0018, as it can be observed in Figure 12d, since the dimensions are the same excepted that it has a sharper nose. In our simulations, for the same relative thickness, profiles with a sharp nose appear to have a slightly lower drag than the NACA airfoil.



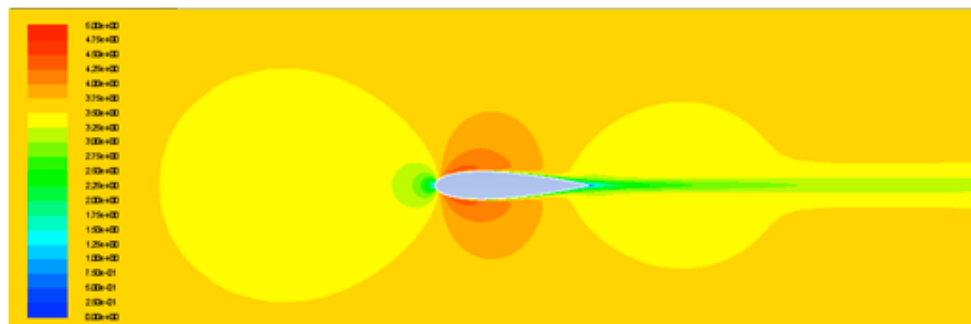
(a)



(b)



(c)



(d)

Figure 12: Velocity distribution around the analyzed profiles: a) $t/c = 26.79\%$ at $c/2$; b) $t/c = 18\%$ at $c/2$; c) $t/c = 18\%$ at $c/3$; d) NACA0018.

Pursuing further our inquiry on the effects of relative thickness, profiles with 15 % and 12 % relative thickness at $c/3$ were tested. We also computed the drag coefficients of thicker NACA profiles: NACA0030 and NACA0035. Figure 13 and Table 4 summarize the results of all simulations.

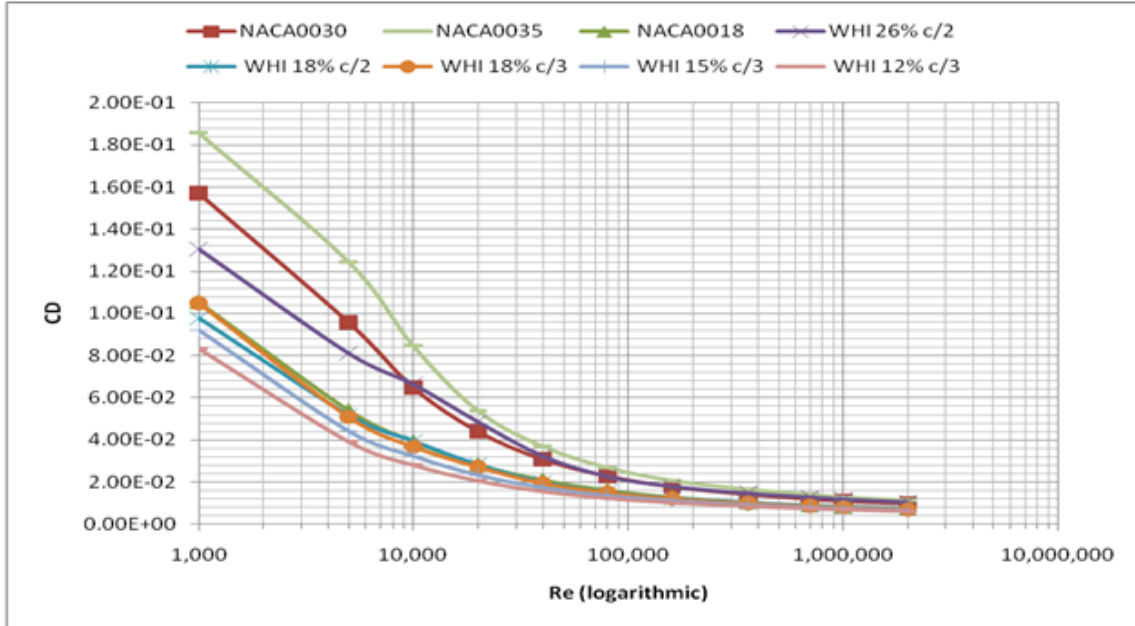


Figure 13: Drag coefficient (C_d) Vs. Reynolds number (logarithmic scale), for all tested profiles, CFD values with correction factor.

Table 4: Experimental and computed data for all analyzed profiles

Re	NACA0018	26.79 % $c/2$	18 % $c/2$	18 % $c/3$	15 % $c/3$	12 % $c/3$	NACA0030	NACA0035
1,000	1.06E-01	1.31E-01	9.78E-02	1.05E-01	9.20E-02	8.33E-02	1.57E-01	1.86E-01
5,000	5.42E-02	8.11E-02	5.17E-02	5.09E-02	4.41E-02	3.91E-02	9.58E-02	1.25E-01
10,000	3.94E-02	6.65E-02	3.94E-02	3.68E-02	3.23E-02	2.80E-02	6.48E-02	8.46E-02
20,000	2.84E-02	4.87E-02	2.81E-02	2.71E-02	2.33E-02	2.05E-02	4.40E-02	5.39E-02
40,000	2.11E-02	3.24E-02	1.98E-02	1.94E-02	1.73E-02	1.55E-02	3.09E-02	3.70E-02
80,000	1.62E-02	2.28E-02	1.50E-02	1.50E-02	1.35E-02	1.23E-02	2.29E-02	2.70E-02
160,000	1.30E-02	1.80E-02	1.23E-02	1.21E-02	1.11E-02	1.02E-02	1.79E-02	2.08E-02
360,000	1.04E-02	1.48E-02	1.02E-02	9.93E-03	9.16E-03	8.48E-03	1.42E-02	1.66E-02
700,000	8.87E-03	1.30E-02	8.91E-03	8.63E-03	7.98E-03	7.43E-03	1.20E-02	1.43E-02
1,000,000	8.19E-03	1.20E-02	8.36E-03	8.04E-03	7.44E-03	6.92E-03	1.10E-02	1.29E-02
2,000,000	7.12E-03	1.06E-02	7.32E-03	7.04E-03	6.52E-03	6.07E-03	9.73E-03	1.14E-02

As it can be expected, lower relative thickness causes lower drag coefficients. However, for a fixed thickness value, a smaller relative thickness means a longer chord length. The drag force is proportional both to C_d and chord length (with same wind velocity and density). Which shape and dimensions causes the lower drag, will be determined using CARDAAV in the following section.

5.2 Blade Arm Drag Calculation

In CARDAAV, the method used to calculate the power loss related to the parasitic drag of the blade arms consist of calculating the local drag force (F_d) on different point along the blade arm lengths using equation 6:

$$F_d = \frac{1}{2} \rho W^2 c C_d \quad (6)$$

Where:

- ρ = The air density
- W = The local relative velocity
- c = The blade arm chord length
- C_d = The airfoil drag coefficient

Then, the local torque (T_d) and average resistive torque (\bar{T}_d) for each blade arm is calculated:

$$T_d = F_d \cdot l \quad (7)$$

$$\bar{T}_d = \frac{1}{2\pi} \int_{-\pi/2}^{\pi/2} \int_{r_T}^r T_d dl d\theta \quad (8)$$

Where:

- l = The distance from the rotation axis
- r_T = The central shaft radius
- r = The blade arm length

The power losses related to the parasitic drag (P_d) for each bade arm is then calculated:

$$P_d = \omega \bar{T}_d \quad (9)$$

Where:

- ω = The rotational speed of the rotor

The total power loss of the rotor is the summation of the power losses of all the blade arms.

For symmetrical streamlined bodies, the drag coefficients mainly depend on the t/c ratio, location of the maximum thickness and the thickness distribution along the chord (including the leading-edge radius and trailing-edge angle) [11]. The influences of those 3 parameters were evaluated in this analysis and similar trends were obtained for the WHI 1500 and WHI 3000. The main difference between the WHI 1500 and WHI 3000 was the parasitic drag values which are smaller for the WHI 1500 due to the shorter struts.

Figures 14 and 15 present the power loss related to the blade arm parasitic drag for the different fairing geometries analyzed, for the WHI 1500 and WHI 3000 respectively.

Pressure drag is highly affected by the thickness, hence for a constant chord length, increasing the t/c ratio would also increase the drag. But for a constant thickness, increasing the t/c ratio reduces the chord length and up to a certain t/c ratio, the reduction of the chord length can compensate the increase in drag coefficient, resulting in a reduction of the power loss due to the blade arm drag. However, past this optimal value, the blade arm chord length reduction is not enough to compensate the drag coefficient increase and increasing the t/c ratio would result in an increase of the power loss related to the blade arms.

Based on this analysis, the optimal t/c ratio seems to be about 30 % for a NACA 4-digit and 18 % for a lenticular cross-section.

v

Figure 14: Power loss for different fairings for the WHI 1500.

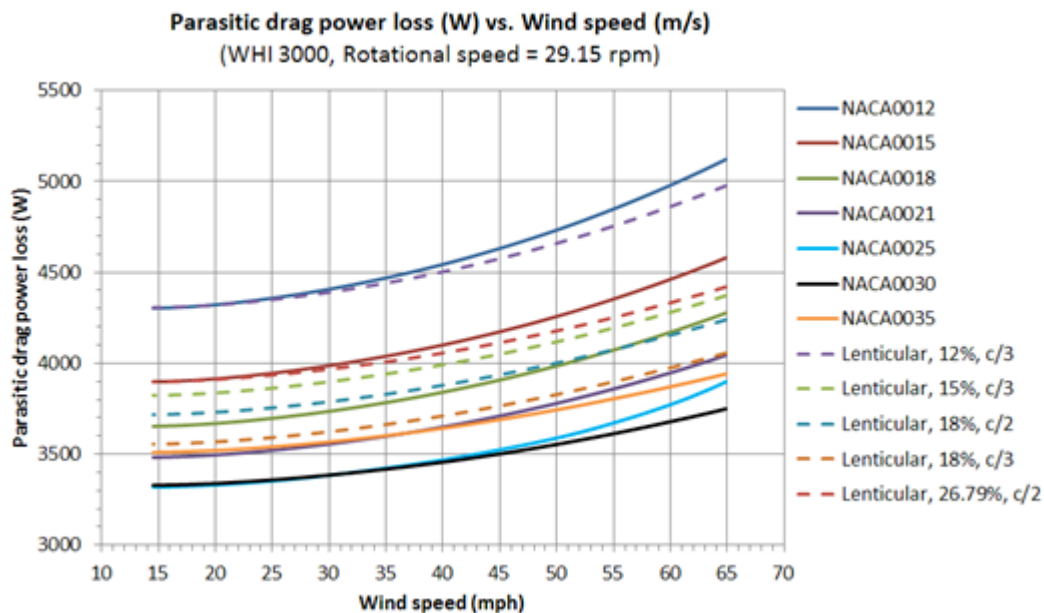


Figure 15: Power loss for different fairings for the WHI 3000.

Moreover, for a similar t/c ratio, moving the maximum thickness location from $c/2$ (50 % of the chord) to $c/3$ (33 % of the chord) reduced the amount of parasitic drag (Figures 16 and 17). As

presented in the preceding section, this can be explained by a smoother pressure gradient passed the maximum thickness location. Hence, for a lenticular cross-section, locating the maximum thickness at $c/3$ should represent a better option than at $c/2$.

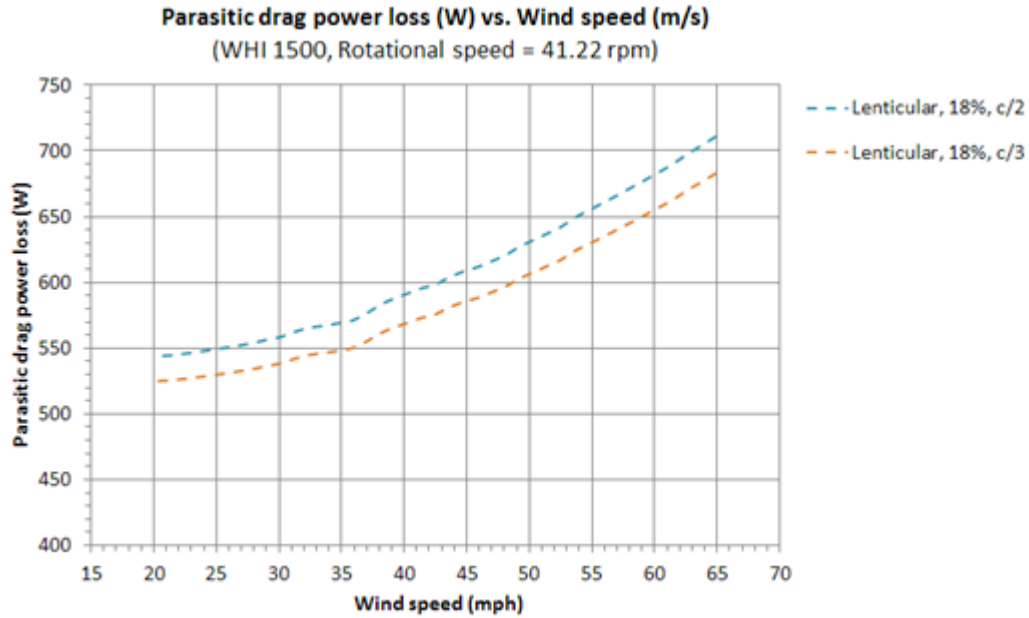


Figure 16: Power loss for a lenticular cross-section with a t/c ratio of 18 % for the WHI 1500.

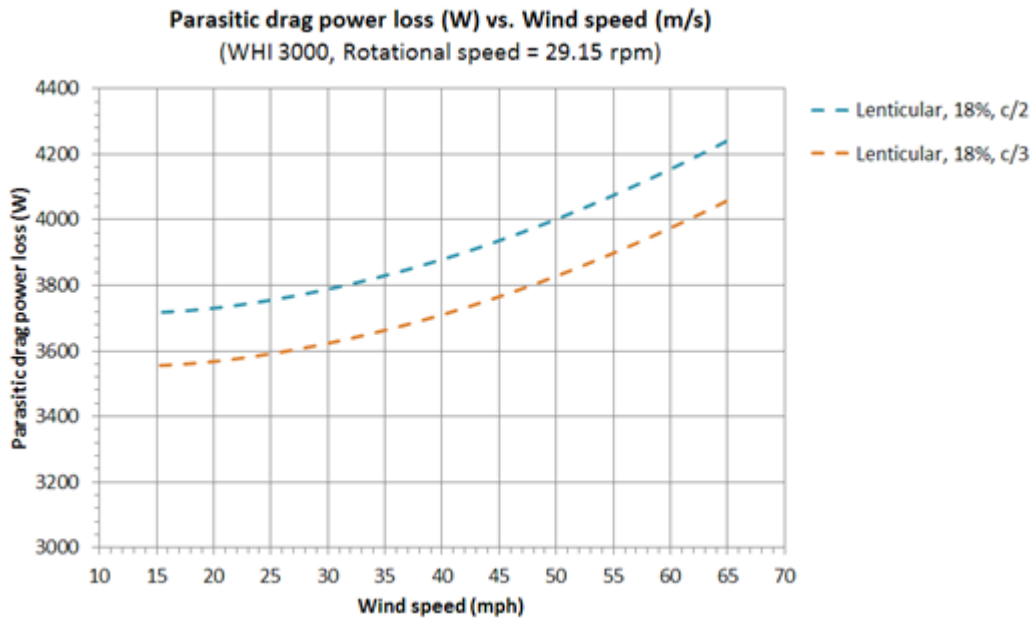


Figure 17: Power loss for a lenticular cross-section with a t/c ratio of 18 % for the WHI 3000.

Based on this analysis, the NACA0030 would produce the lowest parasitic drag at high wind speed, but at low wind speed, the NACA0025 would be slightly better.

For the WHI 3000, changing the blade arm fairing from a lenticular cross-section with $t/c = 26.79\%$ at $c/2$ to a NACA0030 would reduce the amount of power loss due to the parasitic drag of the blade arms by an average of 14.83% over the wind speeds range of 14.54 mph to 64.87 mph. Changing for a NACA0025 would reduce the amount of power loss by an average of 14.18% .

For the WHI 1500, changing the blade arm fairing from a lenticular cross-section with $t/c = 26.79\%$ at $c/2$ to a NACA0030 would reduce the amount of power loss by an average of 13.09% over the wind speeds range of 20.13 mph to 64.87 mph and by 12.95% for a NACA0025.

However, in term of maximum power coefficient, the use of a NACA0025 would represent an increase of 0.5418% for the WHI 3000, compared to 0.5361% for a NACA0030. For the WHI 1500, the use of a NACA0025 would represent an increase of 0.2253% in maximum power coefficient, compared to 0.2024% for a NACA0030.

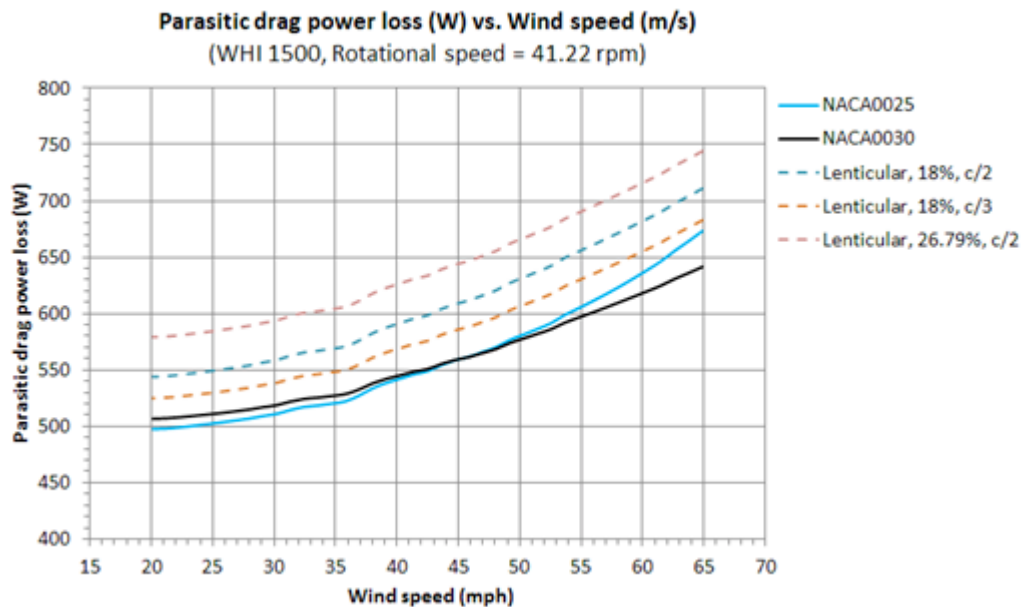


Figure 18: Power loss for different blade arm cross-sections, WHI 1500.

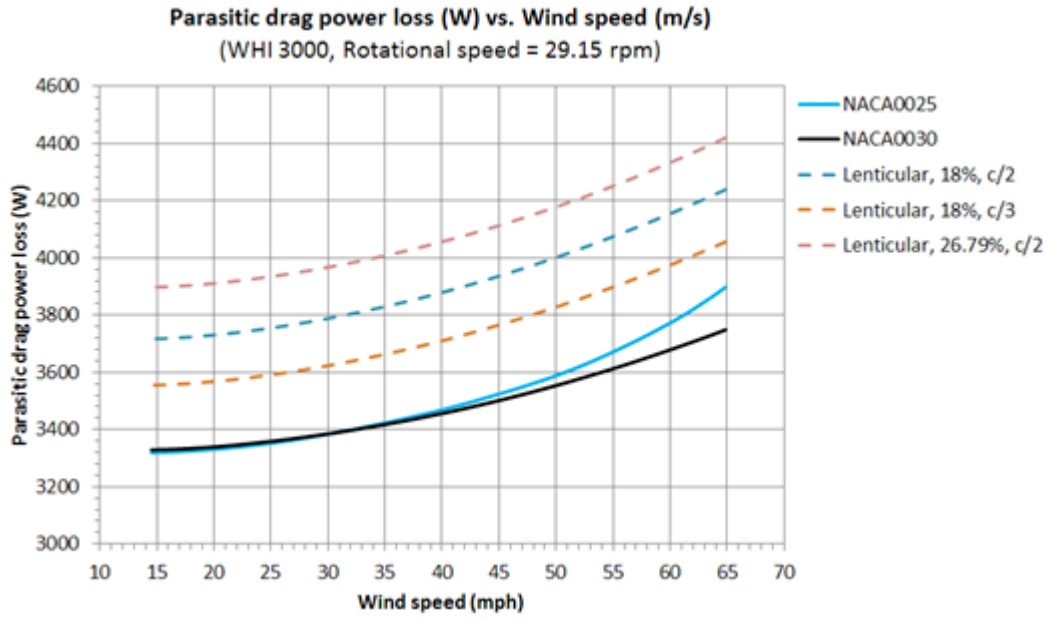


Figure 19: Power loss for different blade arm cross-sections, WHI 3000.

6. EVALUATION OF THE CHANGES TO FAIRING AND BLADE END DESIGN (TASK 3.3)

In order to evaluate the changes in fairing geometry and blade end design, calculations were completed using CARDAAV for the WHI 1500 and WHI 3000, without coupled effect, using NACA0030 airfoil for the fairing geometry, with and without taking into account the blade tip effect i.e. the performance loss associated to the finite span of the blades.

Not considering the blade tip effect would be the equivalent of using properly sized endplates at both extremities of the blades or for the WHI 1500 and WHI 3000 geometries, modifying the end of the blade arm fairing to cover a wider area at the extremities of the blades.

The results are presented in Figures 20 and 21. As we may see from those results, for the WHI 1500, using properly sized endplates at both extremities of the blades could increase the maximum efficiency (power coefficient) by 1.77 %. For the WHI 3000, the maximum efficiency could be increased by 6.24 %. The greater sensitivity to blade tip effect for the WHI 3000 could be explained by the wider rotor aspect ratio (diameter/height ratio) compared to the WHI 1500.

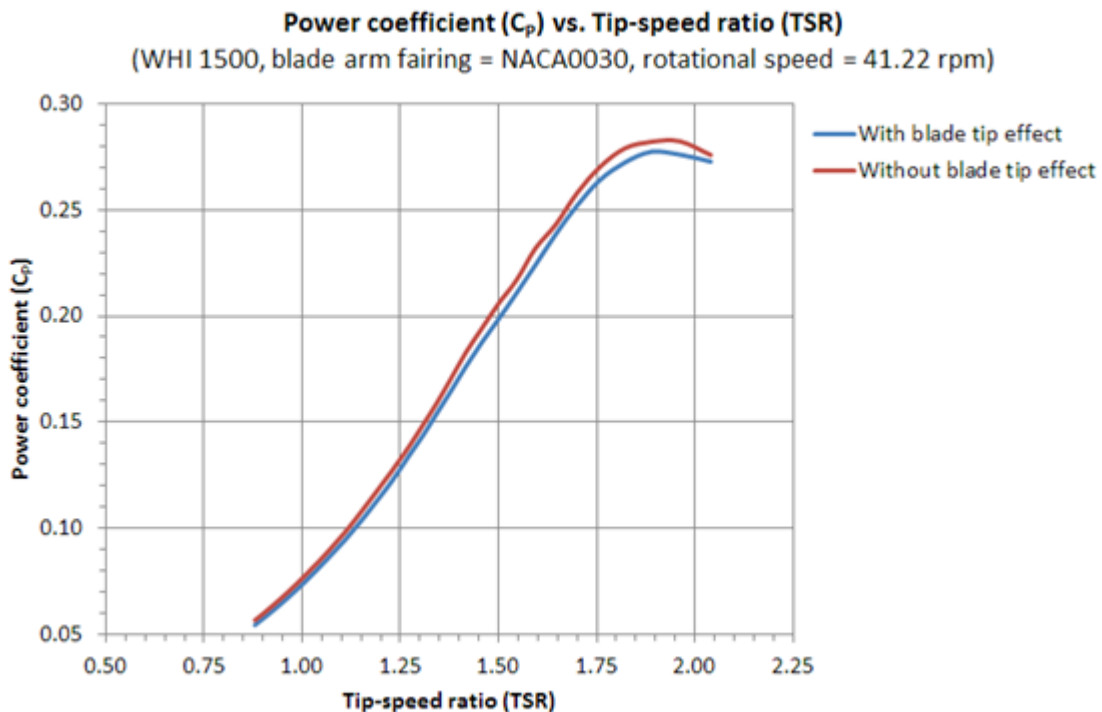


Figure 20: Power coefficient as a function of the tip-speed ratio for the WHI 1500, with and without taking into account the blade tip effect.

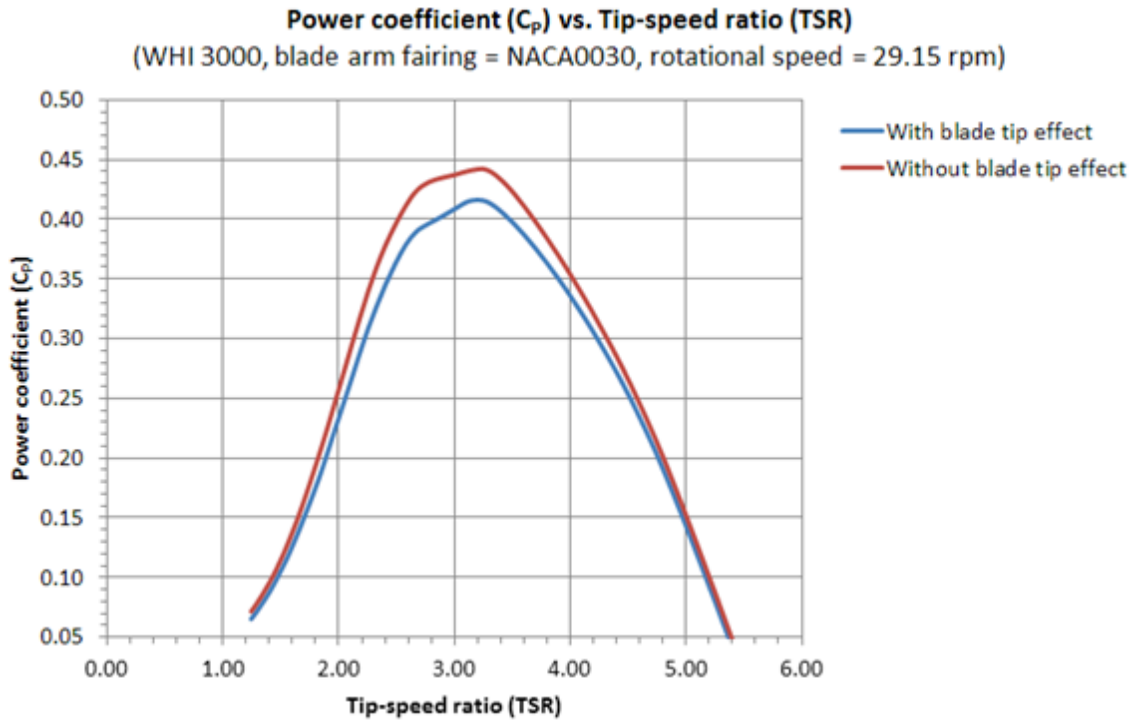


Figure 21: Power coefficient as a function of the tip-speed ratio for the WHI 3000, with and without taking into account the blade tip effect.

7. SIMULATION OF AN ARRAY OF 3 VAWT WITH DIFFERENT PLACEMENT OF COLUMNS (TASK 3.4)

Computational Fluid Dynamics (CFD) is used to simulate the flow around 3 WHI 3000 rotors placed in a linear array. A 2-D simulation is performed therefore blade tip effects are not included. Only top views of the turbines are presented in this report. The wind direction in the figures is from left to right and the rotors are placed top to bottom. The top and bottom rotors are rotating counter clockwise while the middle rotor rotates in the clockwise direction. The objective of this simulation is to study the effect of columns placement which are used as structural support for the turbine. Each column is defined as 10" (0.254 m) diameter circular cross sectional bar. Two kinds of columns placement cases are simulated: in between 2 rotors (case 1) and in front of a turbine (case 2).

The same methodology as described in [12] is used in this work. To be precise, the flow is assumed 2-D and a rotating mesh is used. Unsteady simulations are performed with a time step of 0.003 seconds. The S-A model is used to simulate turbulence. The geometry of one rotor is summarized below (Table 5):

Table 5: Geometry of the WHI 3000 rotor

Number of blades	4
Blade chord	0.9753 m
Rotor Diameter (R)	23.88 m
RPM	29
Blade type	NACA0018

7.1 Case 1 - Columns are Placed in Between Rotors

Figure 22 shows the turbine blades of the 3 rotors and the location of the columns. Note that the central axis is not included. This figure is not to scale and is intended to show a schematic of the geometry. In this simulation only 2 columns are considered: the first one between rotor 1 and rotor 2 and the second between rotor 2 and rotor 3. The location of the column is at a distance of 1.08 rotor radius upstream on the line between the rotors.

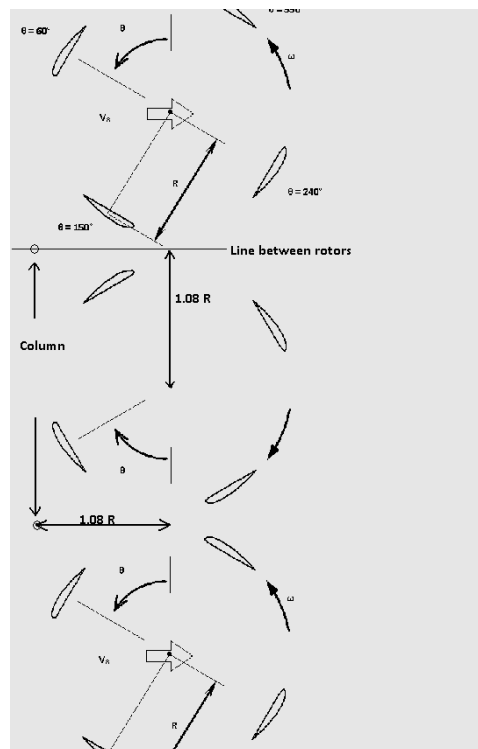


Figure 22: Schematic of a 3-rotor array with columns between arrays.

Figure 23 shows a close up of the mesh used. The column is visible as a black circle on the left side of the figure. The number of elements and nodes are given in Table 6. The elements are concentrated on the blades.

The flow simulation parameters used for the CFD runs are reported in Table 6 for case 1.

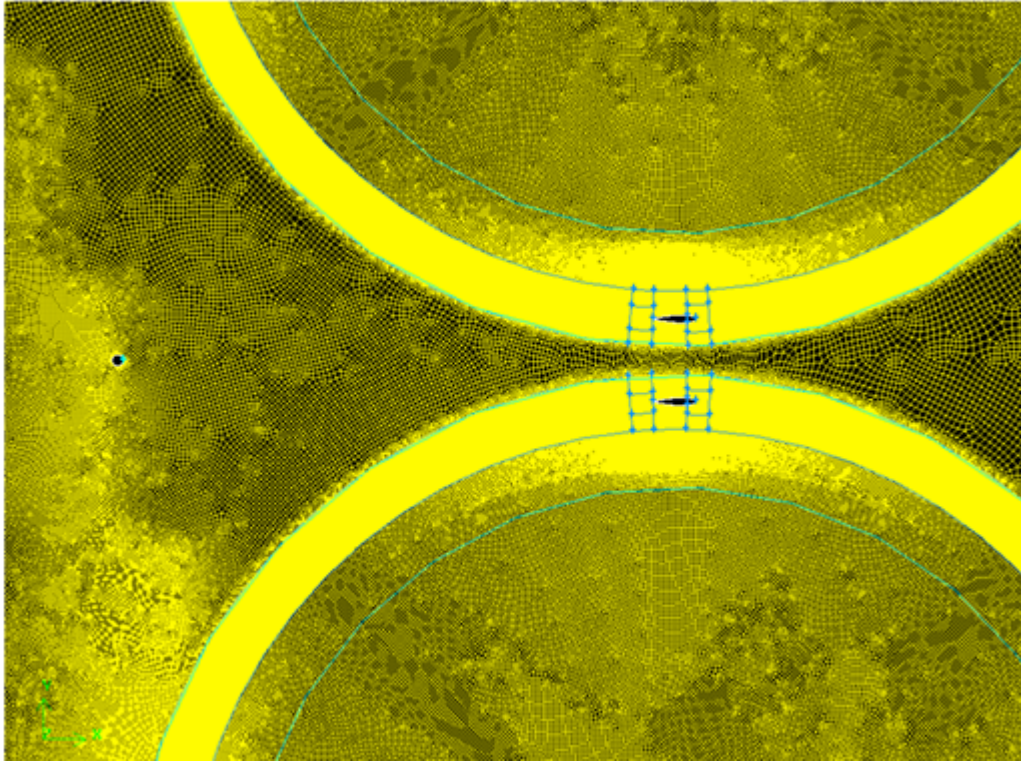


Figure 23: Columns are placed in between rotors.

Table 6: Flow Simulation parameters for case 1

Version	Double precision	
Viscous Model	Spalart-Allmaras (1 equation)	
Solver	Unsteady 2 nd order implicit	
Number of elements	3,002,279	
Number of nodes	3,019,012	
Convergence criteria	Continuity	1e-8
	x-velocity	1e-6
	y-velocity	1e-6
	Nut	1e-6
Time step size	0.003	
Number of processors used to run the simulation	8	

Figures 24 and 25 show iso-contours of average x component of velocity obtained for $TSR = 3$. The color label gives the values of velocity. In Figure 25, the wake behind the column is visible. This wake reduces the wind velocity that reaches the blades and will decrease the overall power coefficient.

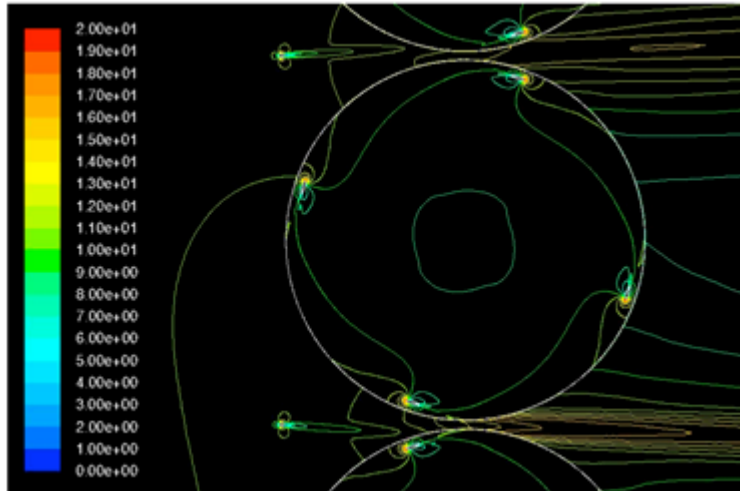


Figure 24: Time average x velocity iso-contours for an array of 3 turbines with columns placed in between rotors.

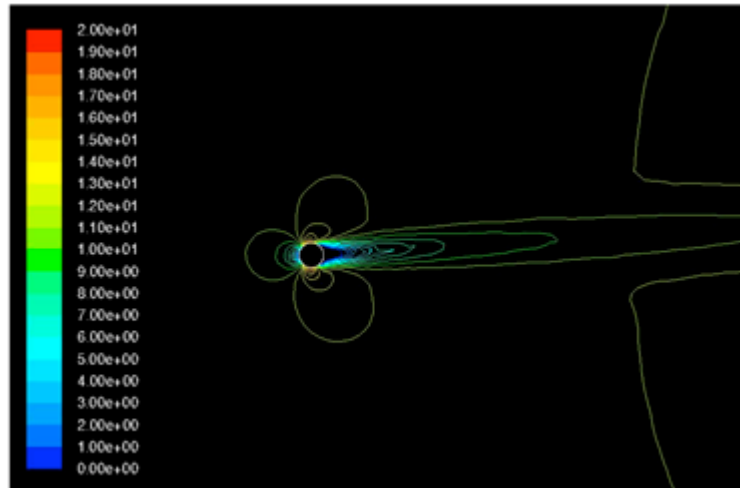
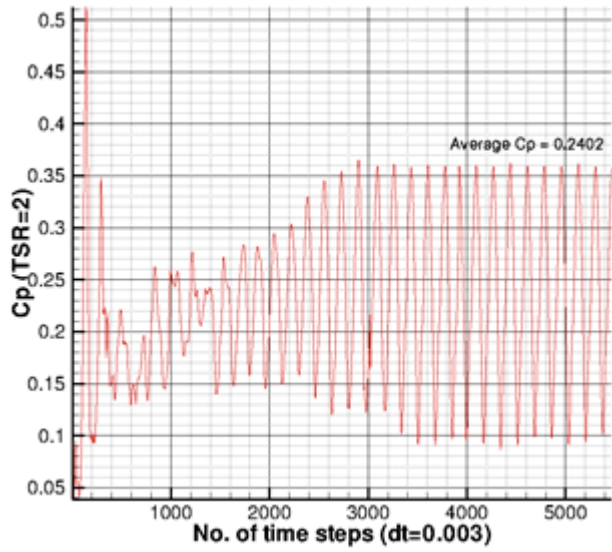
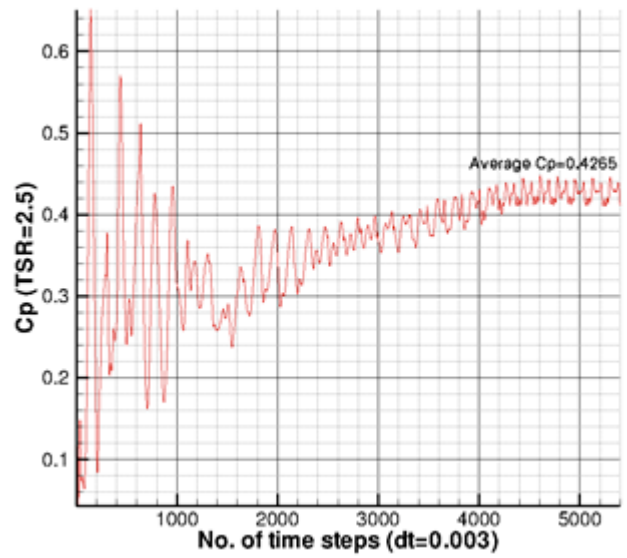


Figure 25: Velocity iso-contours around one column for case 1.

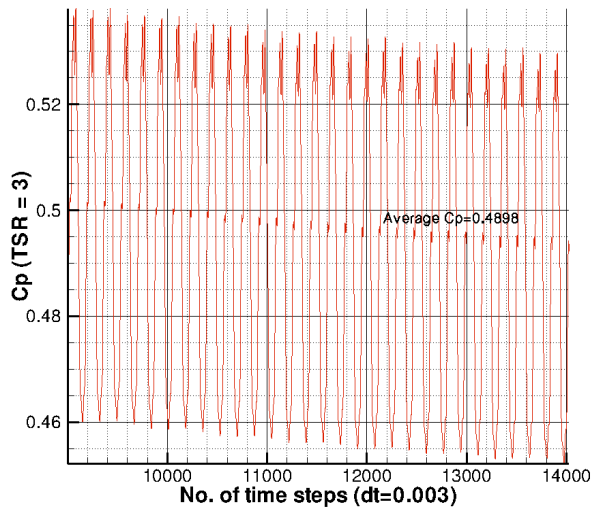
The time history of the power coefficient as a function of iteration number for 3 TSR calculations are reported in Figures 26a, 26b & 26c. To obtain the periodic state at least 5000 iterations are needed for $TSR = 2$ and $TSR = 2.5$. For $TSR = 3$, the total number of time steps needed was 14,000. The average power coefficient is calculated in the 500 iterations. The simulation of case 1 takes around 3 days to run 1,000 time steps on an 8 processors cluster network.



(a)



(b)



(c)

Figure 26: Power coefficient as a function of number of iterations:
 a) at TSR = 2, case 1; b) at TSR = 2.5, case 1; c) at TSR = 3, case 1.

7.2 Case 2 - Columns are Placed in Front of Rotors

Figure 27 shows the location of the column. In this simulation, 3 columns are considered, 1 in front of each rotor, i.e. located at the same distance from the line of the 3 central axes, but moved directly facing the rotor axis. Figure 28 shows the mesh for the instance when the blade is just behind the column.

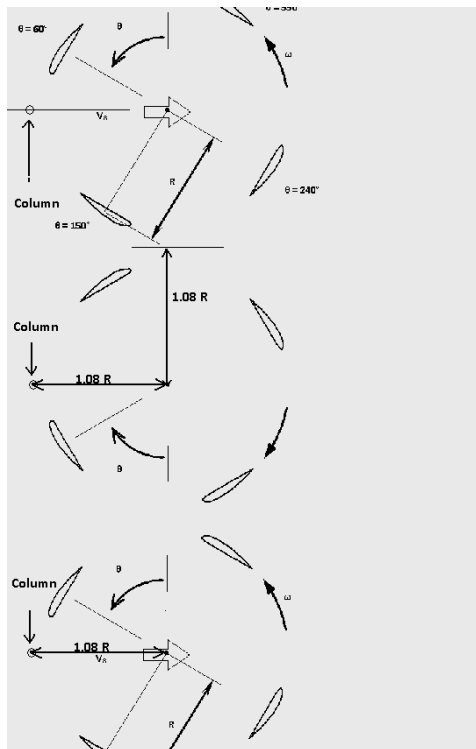


Figure 27: Schematic of a 3-rotor array with columns in front of the rotor.

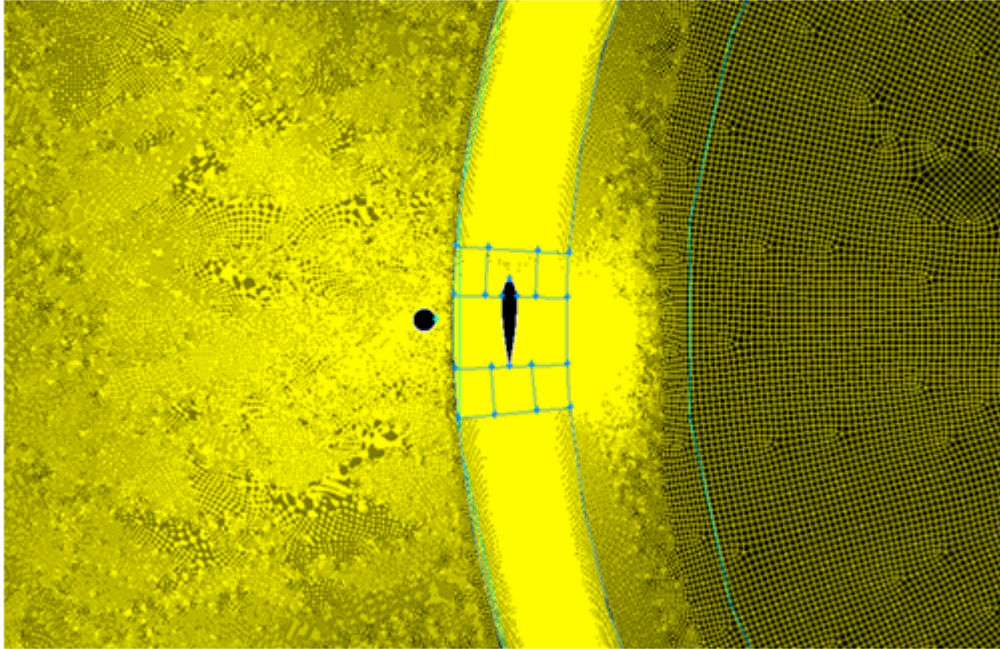


Figure 28: Columns are placed in front of rotors. X coordinates of the column axis is 1.08 rotor radius with respect to rotor axis.

The flow simulation parameters for case 2 are listed in Table 7. The same parameters are used except that the mesh is now different. In this case we had to use 5 million elements to mesh this geometry due to the proximity of the columns to the rotating domain. This mesh is almost double than the mesh used for case 1, but the mesh around the blades is similar.

Table 7: Flow Simulation parameters for case 2

Version	Double precision	
Viscous Model	Spalart-Allmaras (1 equation)	
Solver	Unsteady 2 nd order implicit	
Number of elements	5,057,162	
Number of nodes	5,080,926	
Convergence criteria	Continuity	1e-8
	x-velocity	1e-6
	y-velocity	1e-6
	Nut	1e-6
Time step size	0.003	
Number of processors used to run the job	16	

Figures 29 and 30 show the time average values of the x component of velocity for the case of TSR = 3. Figure 30 shows the wake. Due to the proximity of the rotating domain, the wake looks compressed. This is mainly a visual effect related to the interface region between the rotating mesh and the fixed mesh.

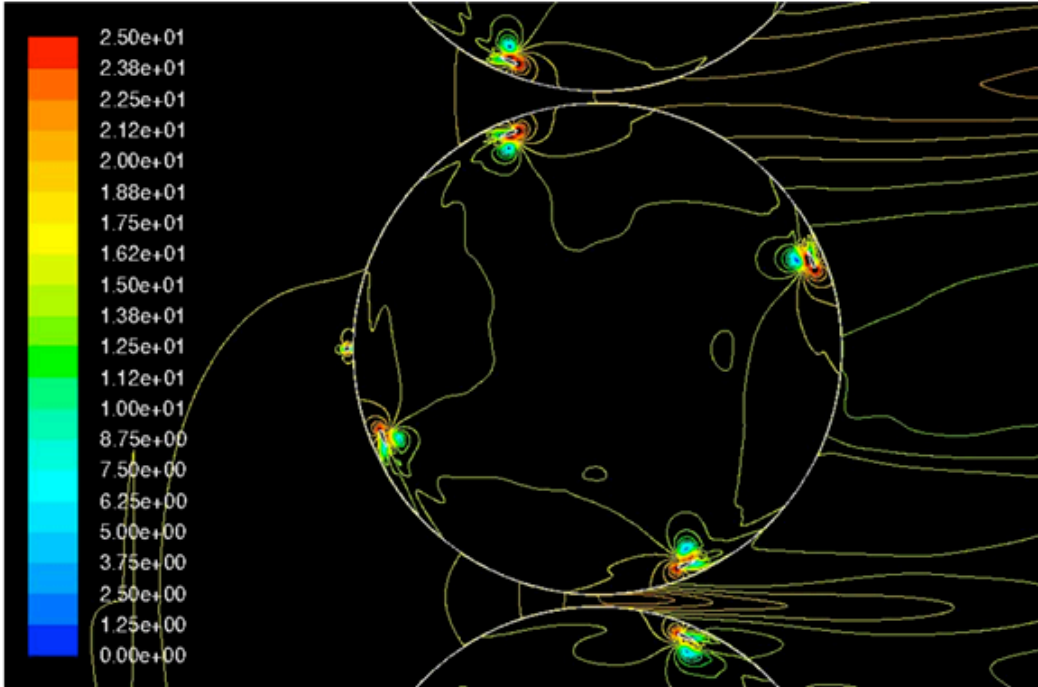


Figure 29: Average x velocity iso-contours for case 2.

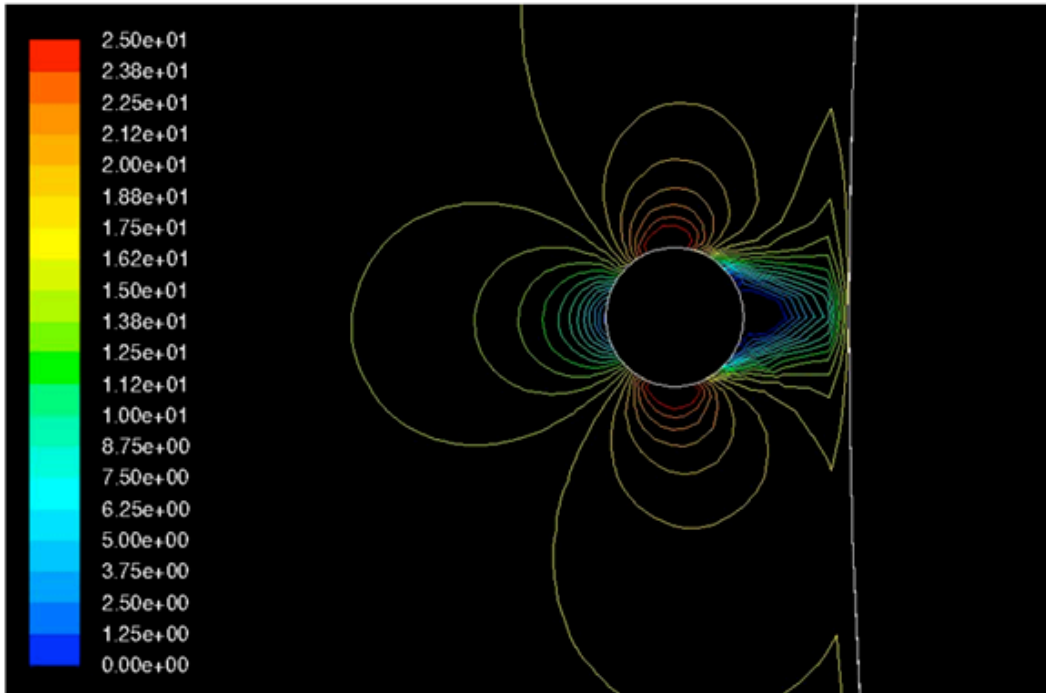
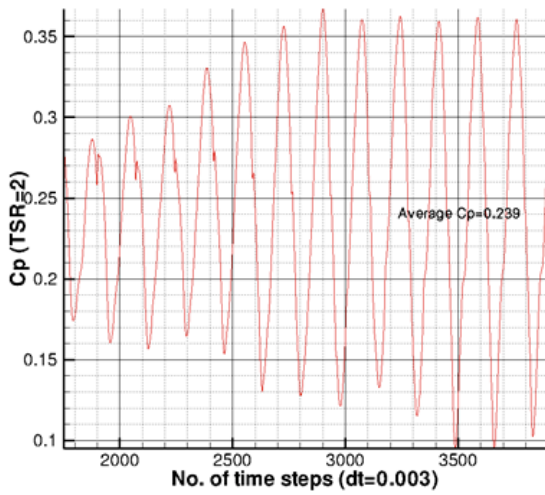
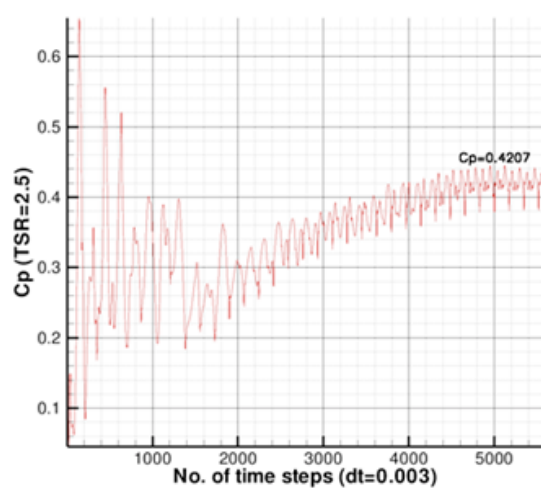


Figure 30: Close up of the average x velocity for one column for case 2.

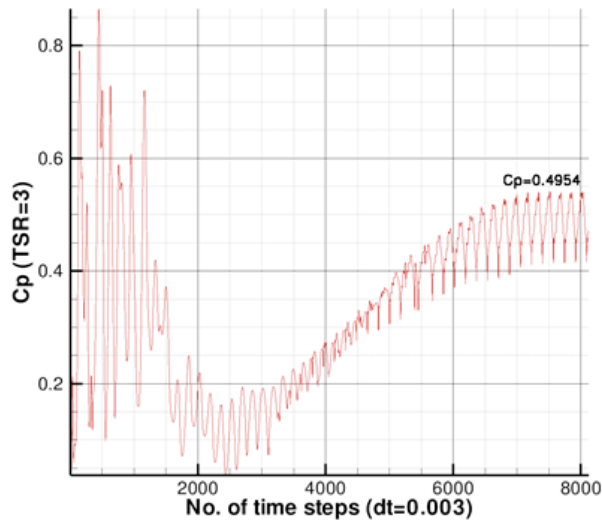
The power coefficient as a function of time is reported in Figures 31a, 31b & 31c for calculations at 3 different TSR values.



(a)



(b)



(c)

Figure 31: Power coefficient as a function of number of iterations:
a) at TSR = 2, case 2; b) at TSR = 2.5, case 2; c) at TSR = 3, case 2.

7.3 Discussion on Case 1 vs. Case 2

In Table 8 the power coefficients are reported for both cases, as well as the case without columns. The case without column is different from the simulation in [12], because a different time step was used. In this report, the case without column was calculated again with a time step of 0.003 similarly to cases 1 and 2.

Table 8: Power coefficient comparison for both column placements

TSR	Case 1	Case 2	Without Column
2.0	0.2402	0.239	0.241
2.5	0.4265	0.4287	--
3.0	0.4898	0.4954	0.496

As seen in the table, both column placements give similar power coefficient values. However, case 1 provides a slightly higher value of the power coefficient than case 2.

The torque on 1 blade is compared for all cases. Figures 32 and 33 show plots of the torque as a function of azimuth angle for a single blade at TSR = 2 and 3, respectively. Note that the azimuthal angle is measured in the clockwise direction, where the zero value is at the bottom, that is when the blade is facing the wind. It can be seen that the columns in front of the blade (case 2) affects the torque near 90 degrees as expected. From these plots, this effect is nevertheless very small. The larger effects are seen at the azimuthal angle of 180 and 250 degrees. At 180 degrees, the blade in case 2 has a higher negative torque than the other 2 configurations. At 250 degrees, case 2 gives a higher torque. Nevertheless the torque curves for all the cases are very similar. Note that the meshes are very different in all cases ranging from 3 to 5 million elements.

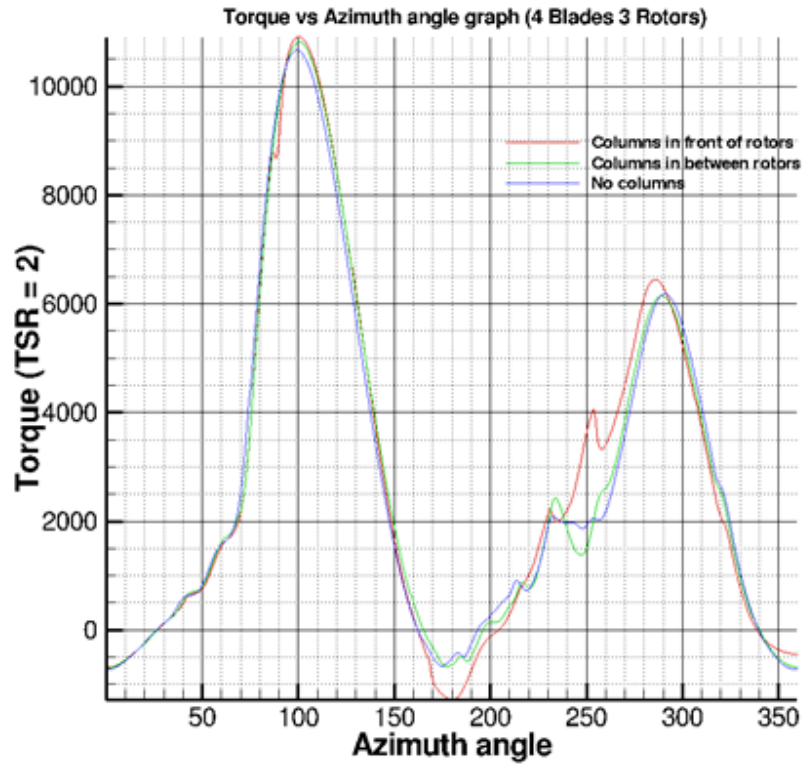


Figure 32: Comparison of torque on 1 blade for all cases at TSR = 2.

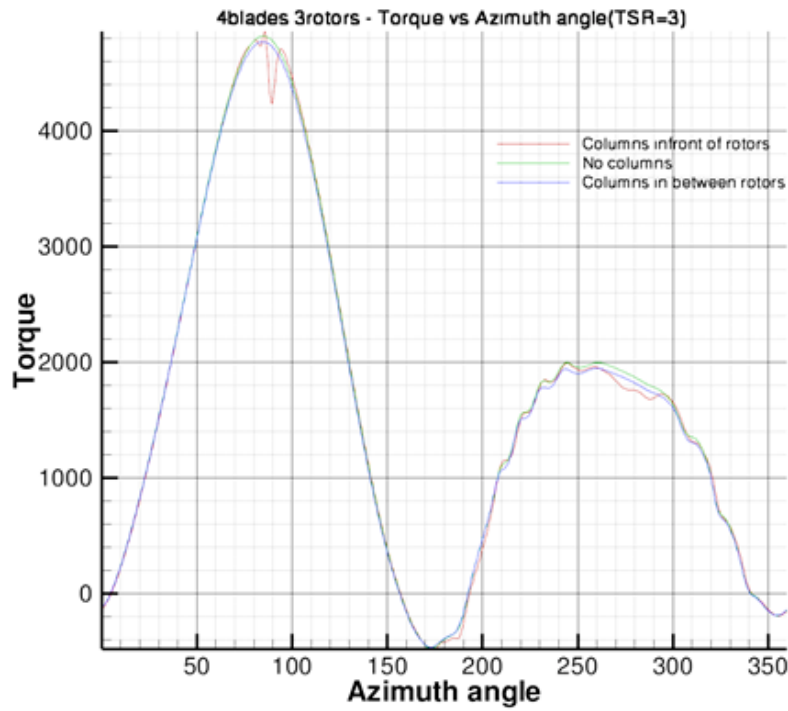


Figure 33: Comparison of torque on 1 blade for all cases at TSR = 3.

8. EFFECT OF WIND DIRECTION ON ROTOR PERFORMANCE (TASK 3.5)

CFD runs based on unsteady Reynolds Average Navier-Stokes equations coupled with the Spalart-Allmaras turbulence model were run using the WHI 3000 model 3-rotor configuration along with the rotor tower. A $120\text{ m} \times 120\text{ m}$ computational domain was modeled with 3 rotors and with the velocity (free stream wind) inlet and pressure outlet (1 atm) boundary conditions as illustrated in Figure 34.

In Figure 34, the wind direction angle γ (gamma) is measured with respect to the normal to the turbine axis as depicted and is taken positive in the clockwise direction in this study. Thus, for $+\gamma$ angles (southwest wind, north being the $+y$ -direction), the inlet and lower (south) domain boundary were used as inlets, while the upper (north) and right side (east) boundaries of the computational domain were modeled as pressure outlets. However, for $-\gamma$ angles (northwest wind), the inlet and upper (north) domain boundaries were used as inlets while the lower (south) and right side (east) boundaries of the computational domain were modeled as pressure outlets.

Results for a total of 15 CFD runs are presented in this report for 5 different wind directions ($\gamma = -30, -15, 0, +15$ and $+30$ degrees) at different TSR values, i.e., $\text{TSR} = 2$ and 3 corresponding to wind speeds of 18.1301 and 12 m/s , respectively, based on co-rotating and counter-rotating (WHI 3000 model) configurations.

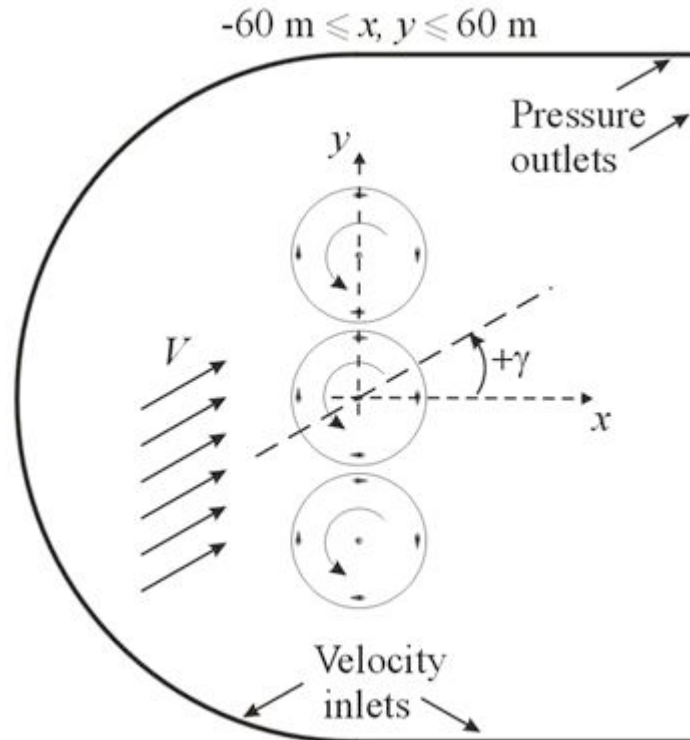


Figure 34: The computational domain illustrating the co-rotating configuration and wind direction angle γ .

Unsteady flow simulations using the Reynolds Average Navier-Stokes equations coupled with the Spalart-Allmaras turbulence model were performed. The computations were performed on a High Performance Computing (HPC) at King Fahd University of Petroleum & Minerals. The HPC houses a high-end 128 compute-node e1350 IBM eServer cluster. Each compute node of the cluster is dual-processor having two 2.0 GHz x3550 Xeon Quad-core E5405 processors totaling a massive 1024-core cluster system. Use of quadrilateral cells and O-type topology were used to mesh the turbine blades, rotors and the computational domain. Figure 35 shows the different views of the computational grid around the turbine. Initially the first-order upwind schemes were used in conjunction with a relaxation factors between 0.4 - 0.7. After 1400 - 1500 iterations, the second-order discretization schemes were employed. The convergence criteria used to monitor solution convergence was based on a 2 to 3 order of magnitude drop in the value of the residuals of mass, momentum, energy and turbulent viscosity.

Table 9: Flow simulation parameters

Rotor Configuration		
Number of blades	4	
Blade chord	0.975 m	
Rotor Diameter (2R)	23.88 m	
RPM (Rotational speed)	29 (3.03687 rad/s)	
Tip speed ratios TSR (Wind speed)	2 (18.13 m/s) and 3 (12 m/s)	
CFD Data		
Version	Double precision solver	
Viscous model	Spalart-Allmaras (1 equation turbulence model)	
Solver	Unsteady 2 nd order implicit	
Number of cells (typical case)	320,987 (2 million after adaption)	
Number of nodes (typical case)	329,309 (2 million after adaption)	
Moving mesh (rad/s)	3.036873	
Free stream velocity (m/s)	18.1301, 12, and 6.8	
Density	1.1774	
Dynamic viscosity	2.173716×10^{-5}	
Convergence criteria	Continuity	$1e^{-6}$
	x-velocity	$1e^{-6}$
	y-velocity	$1e^{-6}$
	Nut	$1e^{-6}$
Time step size	0.003	
Number of processors used	8	
No. of iterations / time step	30 – 60	
Average CPU Time/ time step	120 sec	
Time steps (variable)	3500 - 6500	
Computational time per case	120 – 220 hours (excluding post-processing)	

Starting with a coarse mesh, grid adaption at the solid boundaries was performed to achieve wall-adjacent cell height values of $y^+ \sim 30$ as suggested by mesh guidelines for near-wall modeling approach. Typical coarse grids were of the order of 0.2 million cells. Adapted grids typically consisted of approximately 2 million cells. The key features of the numerical model are listed in Table 9. The average CPU time per iteration listed in Table 9 is based on 4 simultaneous computations on 8 compute nodes the HPC cluster, where each compute node is dual-processor having two 2.0 GHz x3550 Xeon Quad-core E5405 processors and 4 GB of RAM. The average time for each CFD run including its post-processing is around 2 weeks.

Figure 35 shows the details of the computational mesh used in the study where the entire domain is shown in Figure 35a. Mesh details of a single rotor are shown in Figure 35b whereas the mesh around the blades is shown in Figures 35c to 35e. Figure 35e shows grid refinement in regions around the blades and in between the rotors as compared to Figure 35d to allow more accurate resolution of flow gradients.

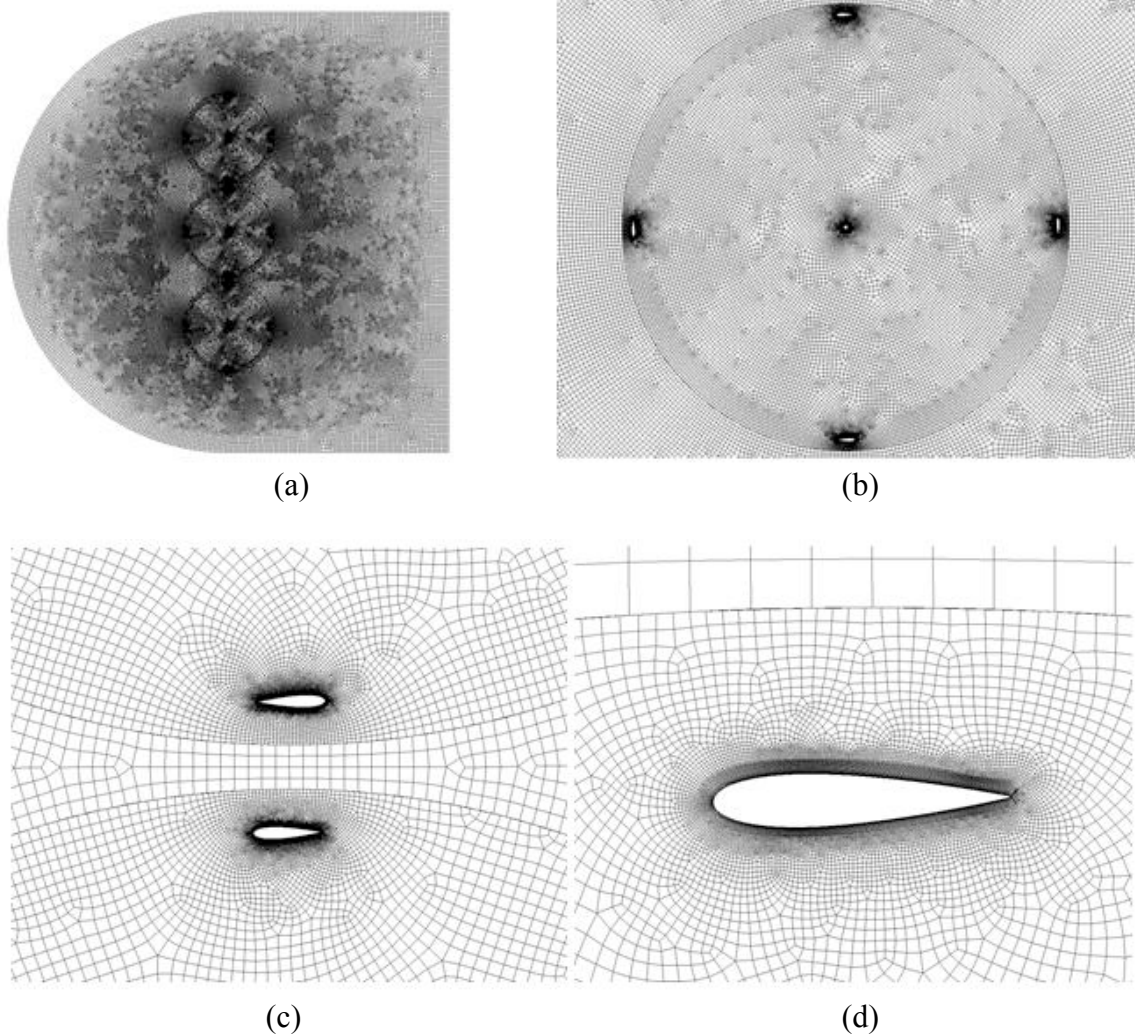
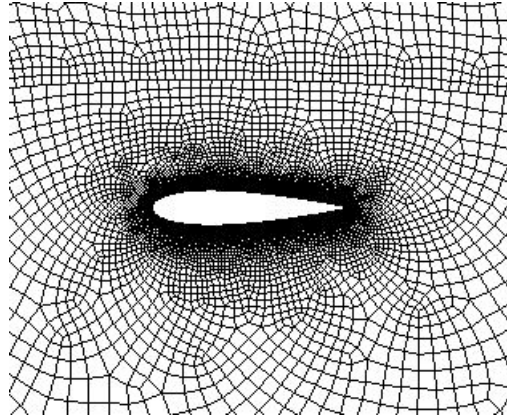


Figure 35: Details of the computational mesh used in the study.

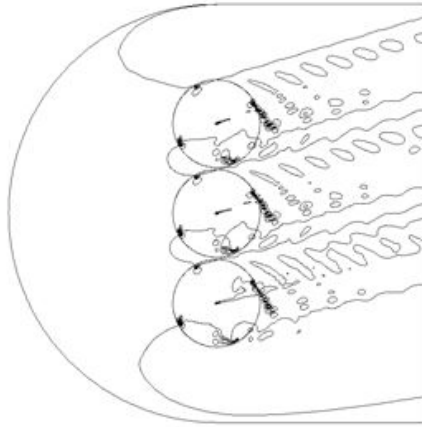


(e)

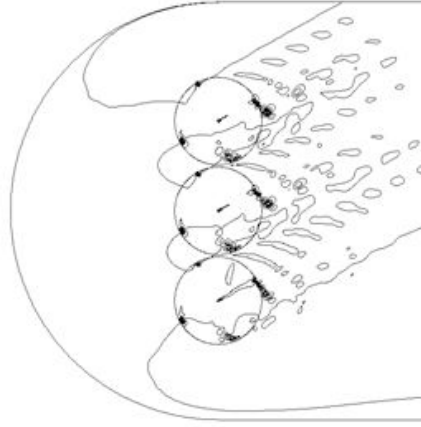
Figure 35 (continued): Details of the computational mesh used in the study.

8.1 Case 1 - Co-Rotating Rotors

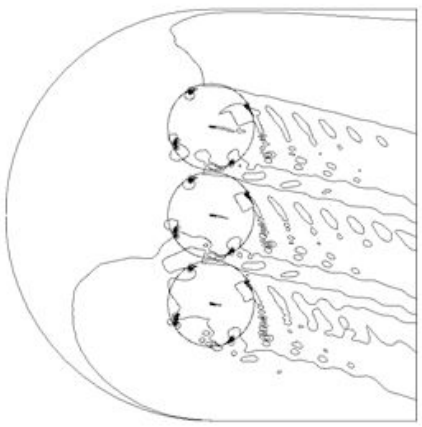
Figure 36 shows the effect of the wind direction on the trailing vortices shed from the turbine rotors based on the current CFD simulations. The figure shows contours of velocity magnitude. Figures 37 and 38 show more detailed contour plots of velocity magnitude for the south- and north-westerly wind directions, respectively. The resulting power coefficient C_p history (time) plot for the south- and north-westerly wind directions and TSR values of 2 and 3 are presented in Figures 39 through 42. The power coefficient C_p history (time) plots show that south-westerly wind directions introduces a lag in C_p values which is more prominent at lower TSR values while north-westerly directions show an opposite trend. In addition, it is seen that a decreasing (more northerly) wind direction tends to increase the average power coefficient C_p by a few percent. The average values of the torque (moment) coefficient C_m and the power coefficient C_p for the cases studied are listed in Table 10. Table 11 lists the reference values used in the CFD simulations.



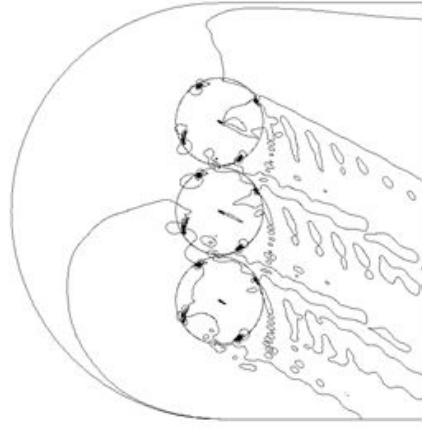
(a) Wind direction angle $\gamma = +15$ degrees.



(b) Wind direction angle $\gamma = +30$ degrees.

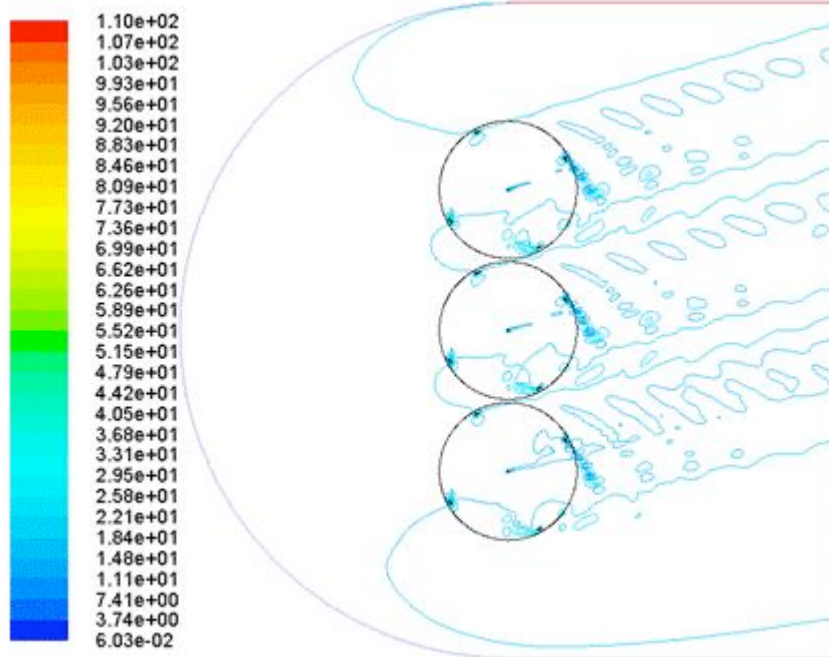


(c) Wind direction angle $\gamma = -15$ degrees.

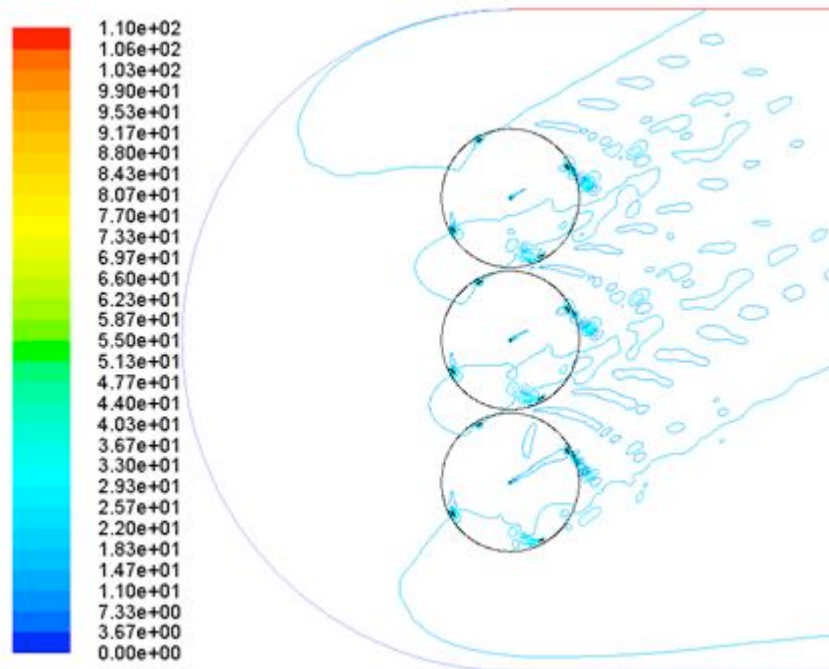


(d) Wind direction angle $\gamma = -30$ degrees.

Figure 36: Effect of wind direction on the trailing vortices shed from the turbine rotors.

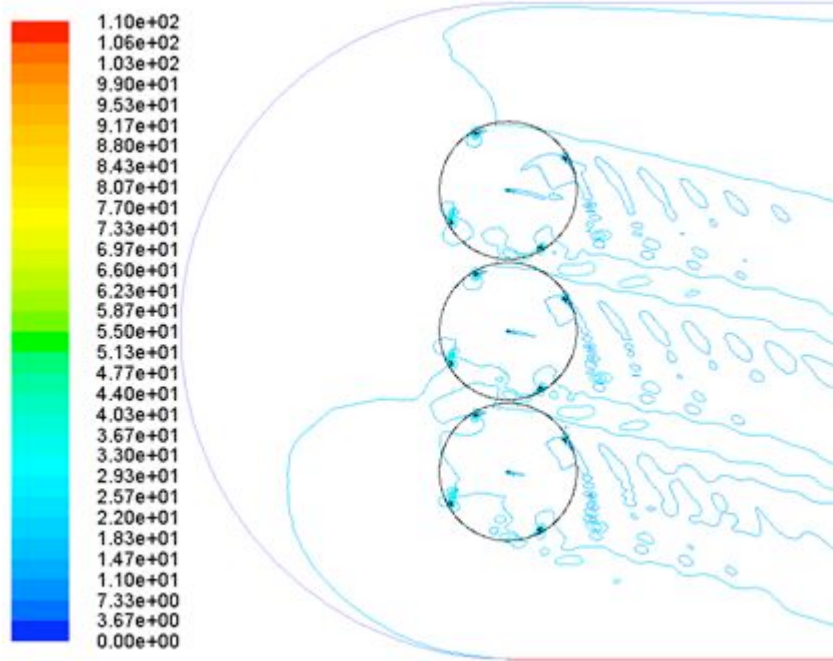


(a) Wind direction angle $\gamma = +15$ degrees.

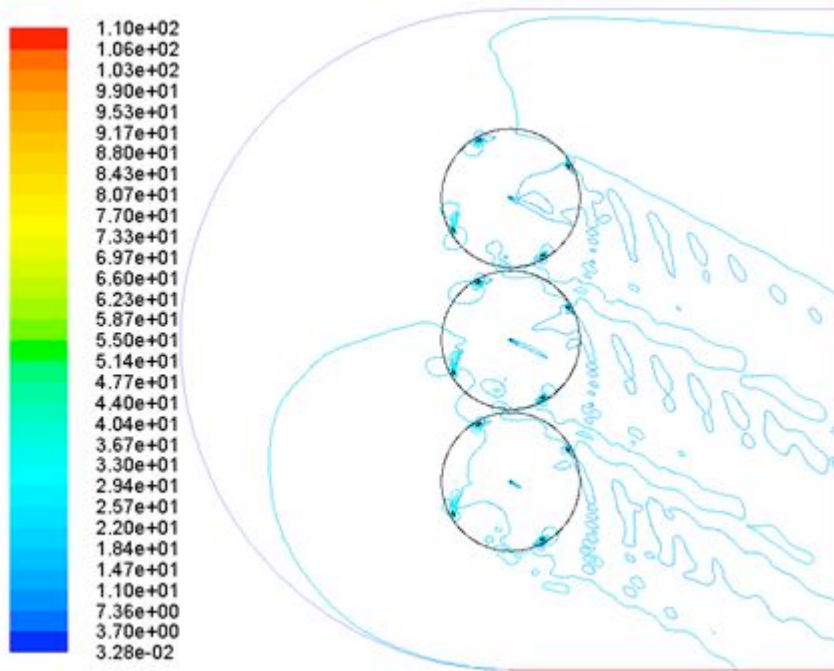


(b) Wind direction angle $\gamma = +30$ degrees.

Figure 37: Contour plot of velocity magnitude for south-westerly wind directions (Wind speed = 18.1301 m/s).



(a) Wind direction angle $\gamma = -15$ degrees.



(d) Wind direction angle $\gamma = -30$ degrees.

Figure 38: Contour plot of velocity magnitude for north-westerly wind directions (Wind speed = 18.1301 m/s).

Effect of Wind Direction on Model 3000 Performance (V = 18 mps, TSR = 2)

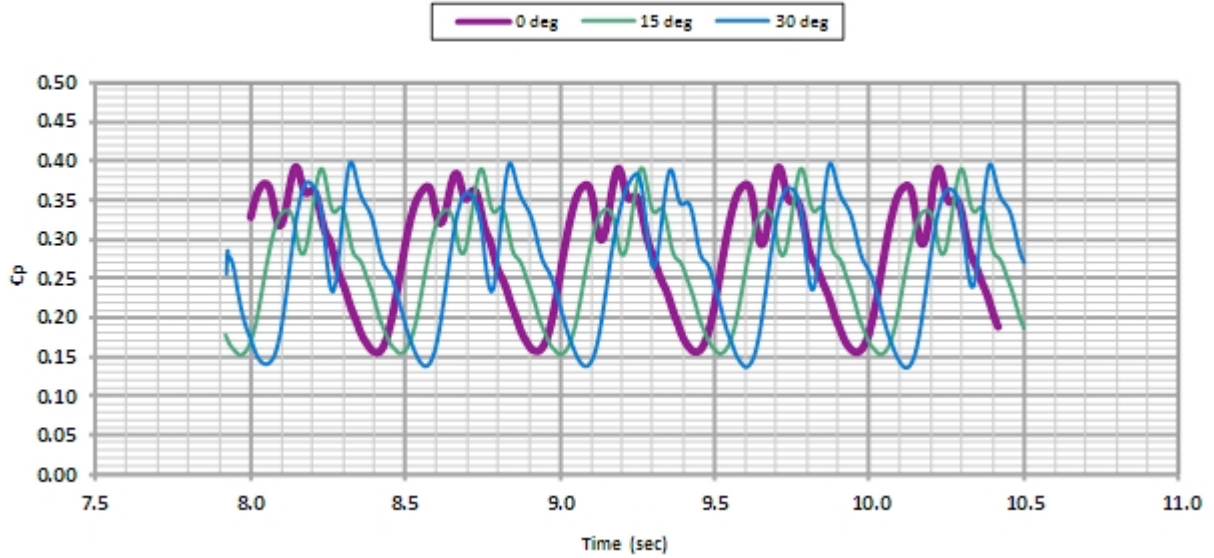


Figure 39: Plot of power coefficient for south-westerly wind directions (Wind speed = 18.1301 m/s, TSR = 2).

Effect of Wind Direction on Model 3000 Performance (V = 18 mps, TSR = 2)

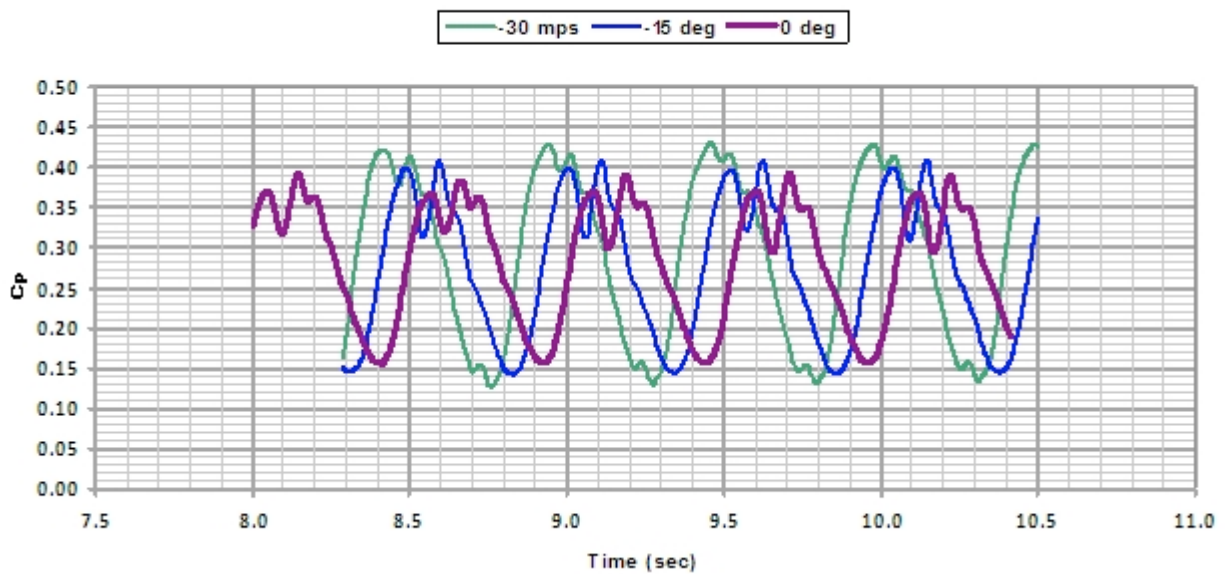


Figure 40: Plot of power coefficient for north-westerly wind directions (Wind speed = 18.1301 m/s, TSR = 2).

Effect of Wind Direction on Model 3000 Performance (V = 12 mps, TSR = 3)

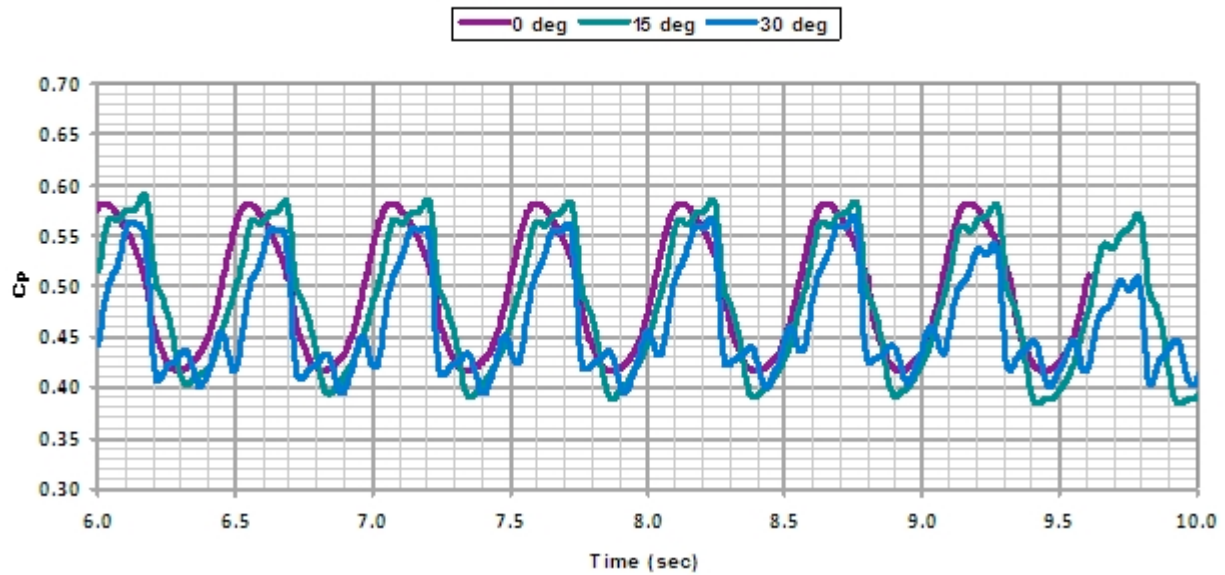


Figure 41: Plot of power coefficient for south-westerly wind directions (Wind speed = 12 m/s, TSR = 3).

Effect of Wind Direction on Model 3000 Performance (V = 12 mps, TSR = 3)

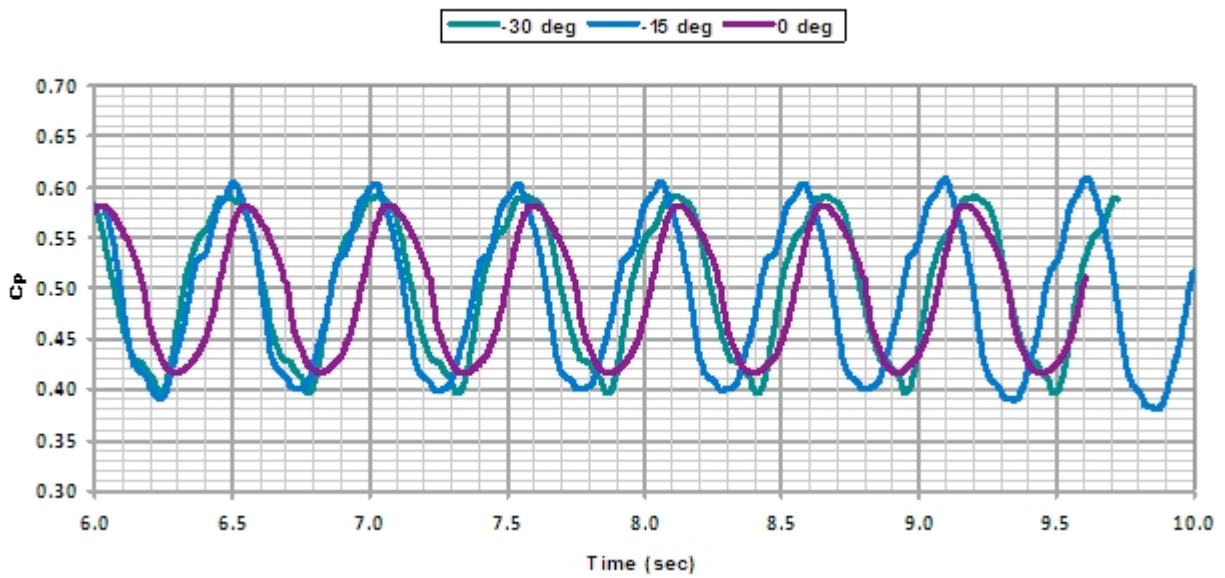


Figure 42: Plot of power coefficient for north-westerly wind directions (Wind speed = 12 m/s, TSR = 3).

Table 10: Torque and power coefficient predictions using CFD

TSR	Wind Speed	γ (deg)	C_m	C_P	% C_{P0}
2.00	18.13 m/s	-30.00	43.491	0.290	3.349
	40.56 mph	-15.00	42.131	0.281	0.116
		0.00	42.082	0.281	--
		15.00	40.812	0.272	-3.018
		30.00	40.950	0.273	-2.690
TSR	Wind Speed	γ (deg)	C_m	C_P	% C_{P0}
3.00	12.10 m/s	-30.00	50.771	0.511	3.540
	27.07 mph	-15.00	49.199	0.496	0.335
		0.00	49.035	0.494	--
		15.00	48.083	0.484	-1.942
		30.00	45.728	0.461	-6.745

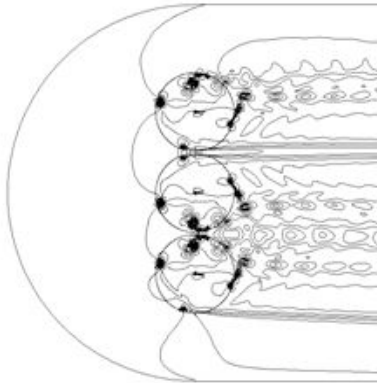
Table 11: Reference values used in the CFD simulations

Reference values

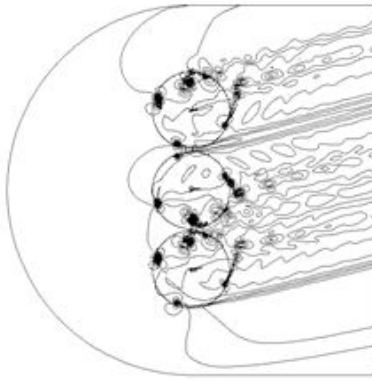
Length	0.975 M
Density	1.1774 kg/m ³
Viscosity	2.17372E-05 kg-m/s
Depth	1 M
Velocity	12/18.1301 m/s
Temperature	288.16 K

One possible explanation for the increase in the power coefficient values for northerly wind directions is as follows. It can be seen that with an increase in wind direction, the advancing blades (moving into the wind) of a rotor encounter turbulent wake of adjacent rotor blades. Moreover, it can also be seen that for higher values of positive (southerly) wind direction angles [Figures 36a and 36b], the blades experience an increased angle of attack in the advancing half and therefore increased separation and lower values of power coefficient. In contrast, the negative values of wind direction (northerly) angles [Figures 36c and 36d], result in decreased angle of attack in the advancing half and therefore decreased separation and thus higher values of power coefficient. This important finding suggests that the turbine could be sited to take advantage of the northerly wind (with reference to the 3-rotor turbine axis) and thus, preserve the omni-direction advantage of VAWT in an overall sense.

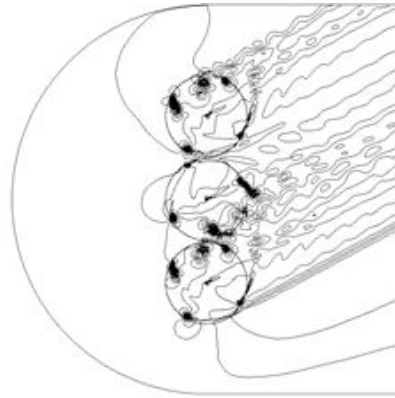
8.2 Case 2 - Counter-Rotating Rotors (WHI 3000)



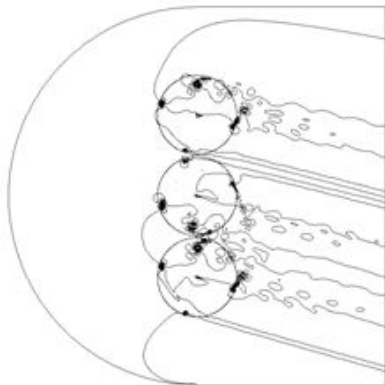
(a) Wind direction angle $\gamma = 0$ degrees.



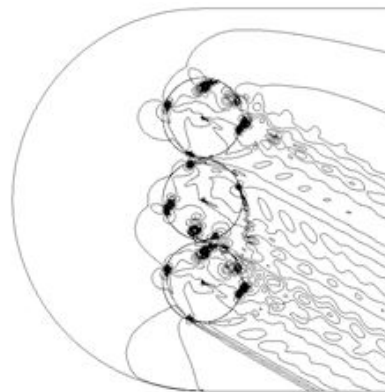
(b) Wind direction angle $\gamma = +15$ degrees.



(c) Wind direction angle $\gamma = +30$ degrees.



(d) Wind direction angle $\gamma = -15$ degrees .



(e) Wind direction angle $\gamma = -30$ degrees.

Figure 43: Effect of wind direction on the trailing vortices shed from counter-rotating turbine rotors.

CFD simulation results for the case of counter-rotating rotors configuration or the WHI 3000 multiple rotors model are presented in Figures 43 through 48 in this section. The figures show contours of velocity magnitude for the different westerly wind directions. Figures 44 through 46 show more detailed contour plots of velocity magnitude. The resulting power coefficient C_P history (time) plots for the south- and north-westerly wind directions for TSR value 2 are presented in Figures 47 and 48, respectively. The power coefficient C_P history (time) plots show that south-westerly wind directions introduces a lag in C_P values, while north-westerly directions show an opposite trend. In addition, it is seen that a smaller value of north-westerly wind direction tends to increase the average power coefficient C_P to within 1 %, which is seen to diminish with increasing north-westerly wind directions. The average values of the torque (moment) coefficient C_m and the power coefficient C_P for the counter-rotating rotors configuration obtained through CFD simulations are listed in Table 12.

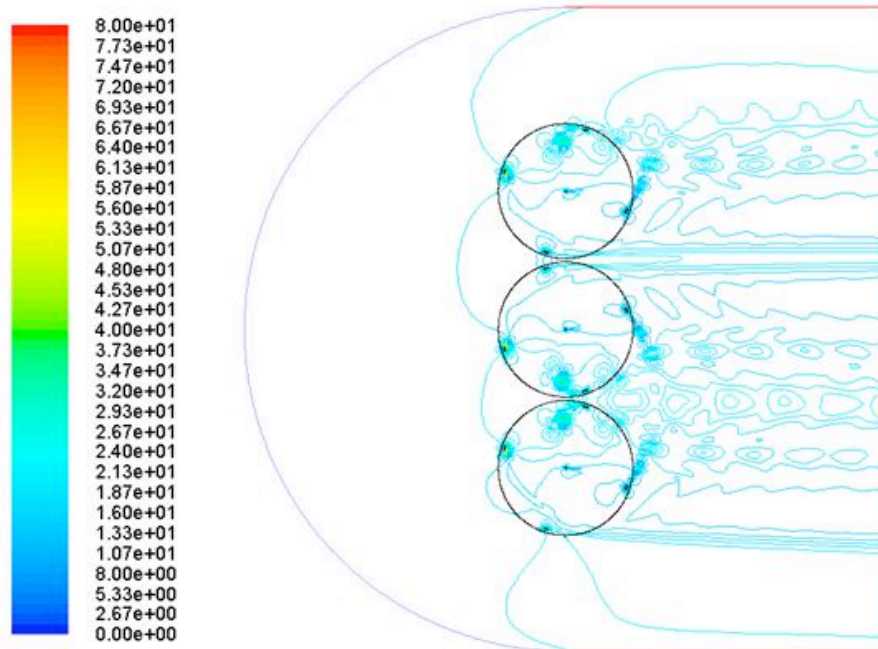
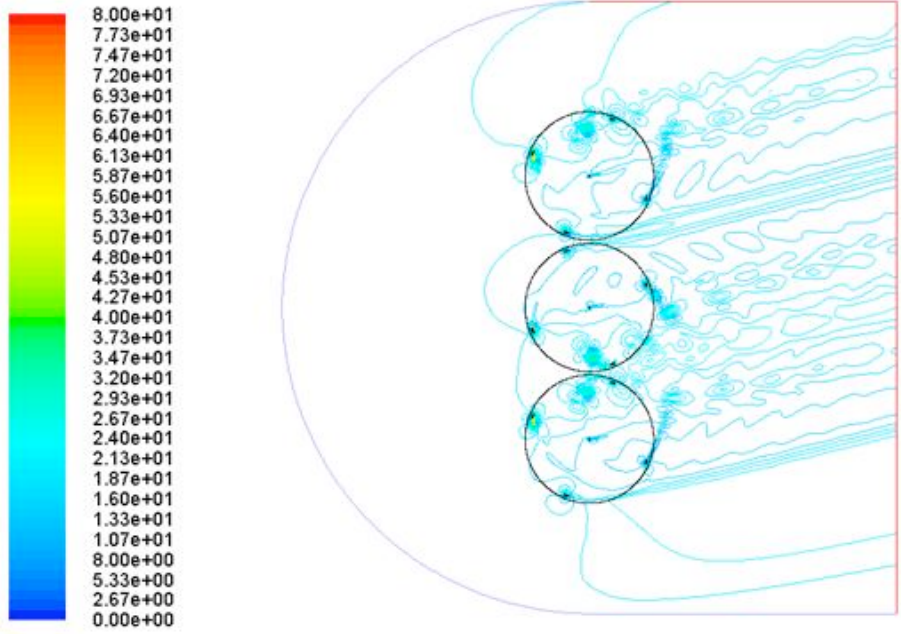
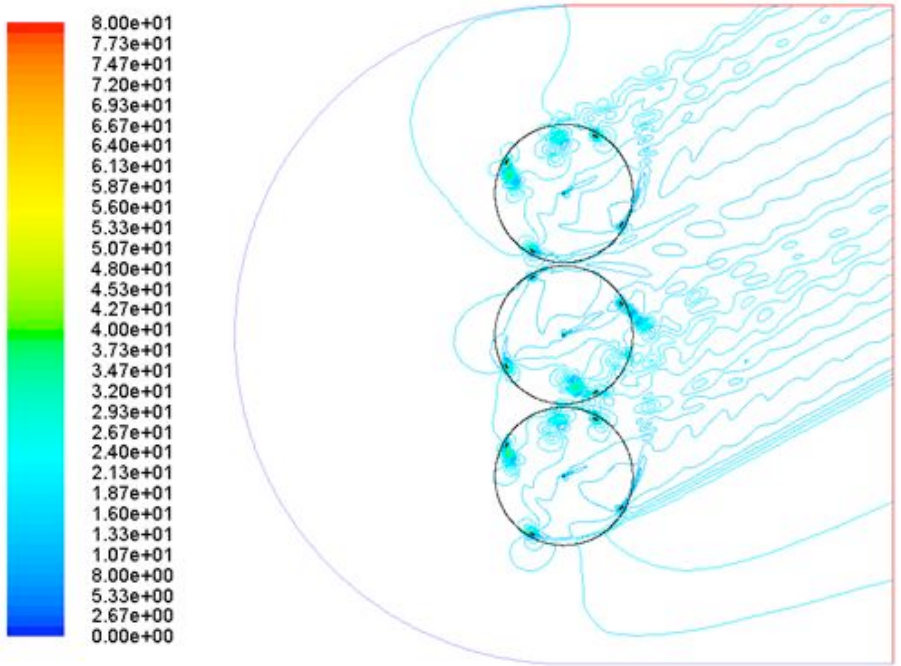


Figure 44: Contour plot of velocity magnitude for westerly wind (Wind speed = 18.1301 m/s).

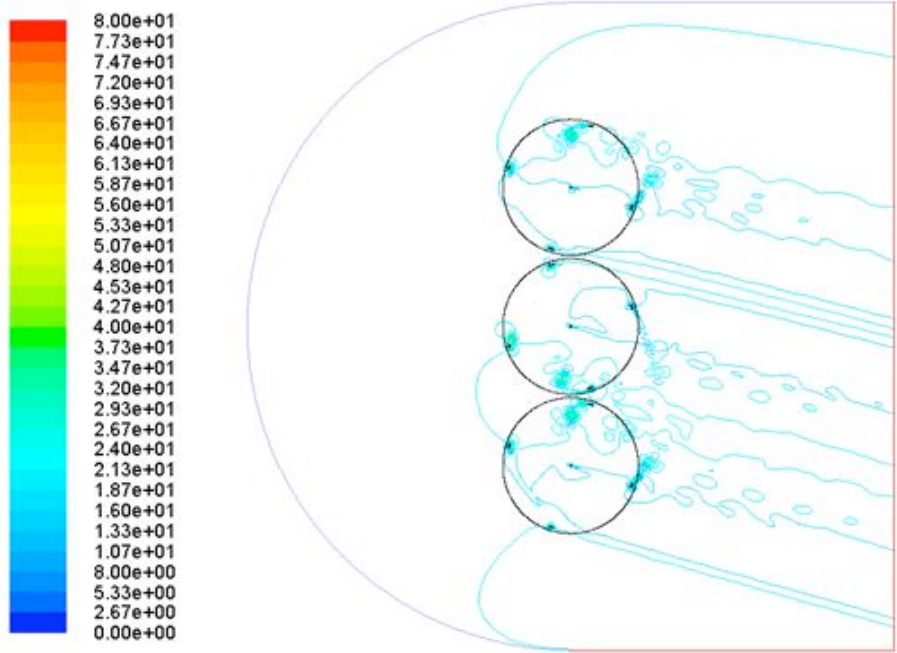


(a) Wind direction angle $\gamma = +15$ degrees.

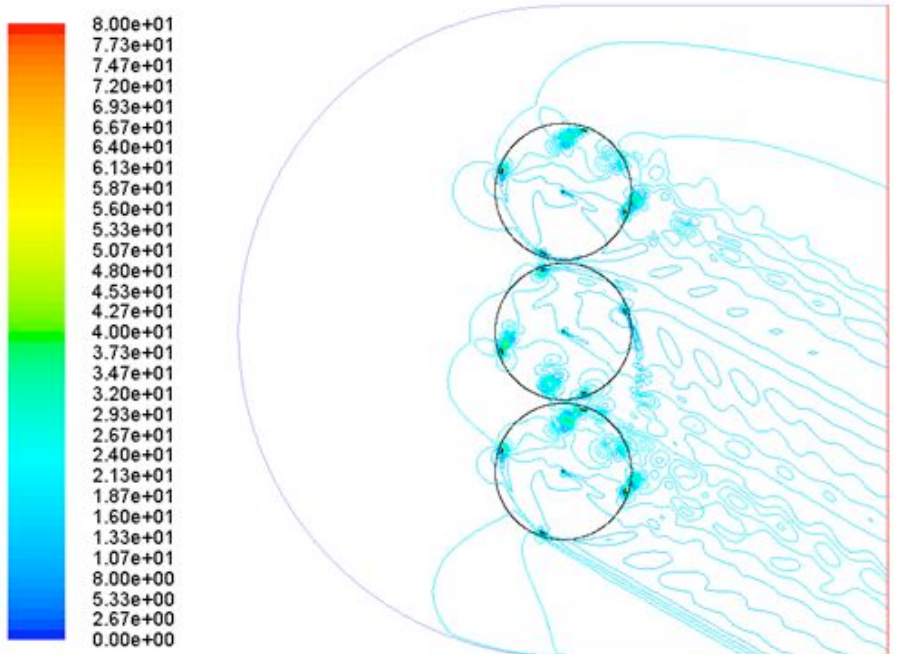


(b) Wind direction angle $\gamma = +30$ degrees.

Figure 45: Contour plot of velocity magnitude for south-westerly wind directions (Wind speed = 18.1301 m/s).



(a) Wind direction angle $\gamma = -15$ degrees.



(b) Wind direction angle $\gamma = -30$ degrees.

Figure 46: Contour plot of velocity magnitude for north-westerly wind directions (Wind speed = 18.1301 m/s).

Effect of Wind Direction on Model 3000 Performance ($V = 18$ mps, $TSR = 2$)

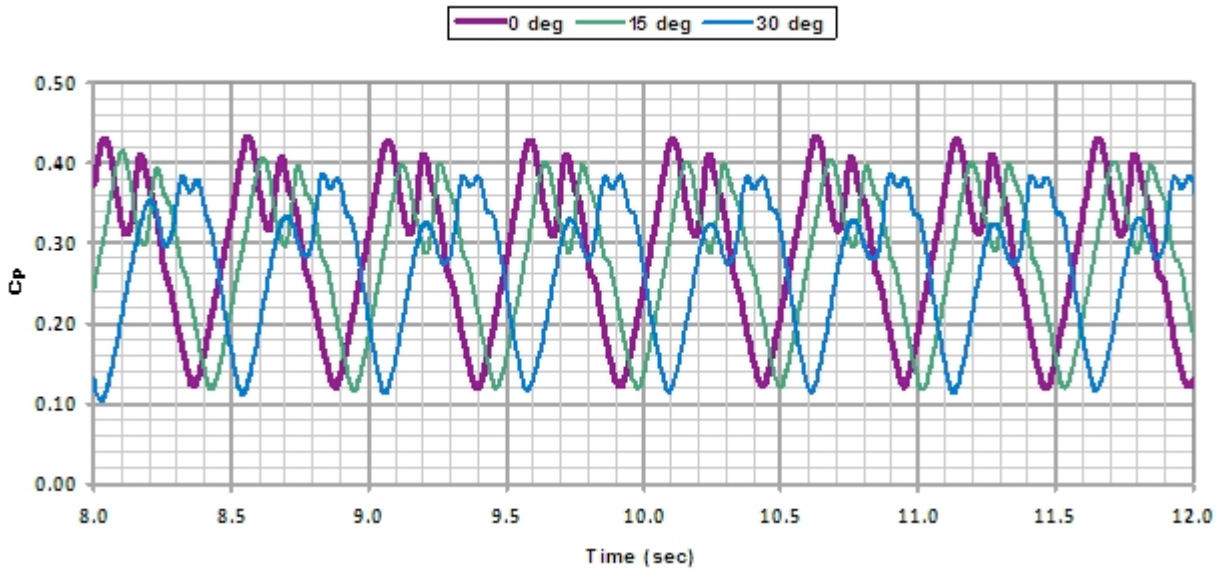


Figure 47: Plot of power coefficient for south-westerly wind directions (Wind speed = 18.1301 m/s, $TSR = 2$).

Effect of Wind Direction on Model 3000 Performance ($V = 18$ mps, $TSR = 2$)

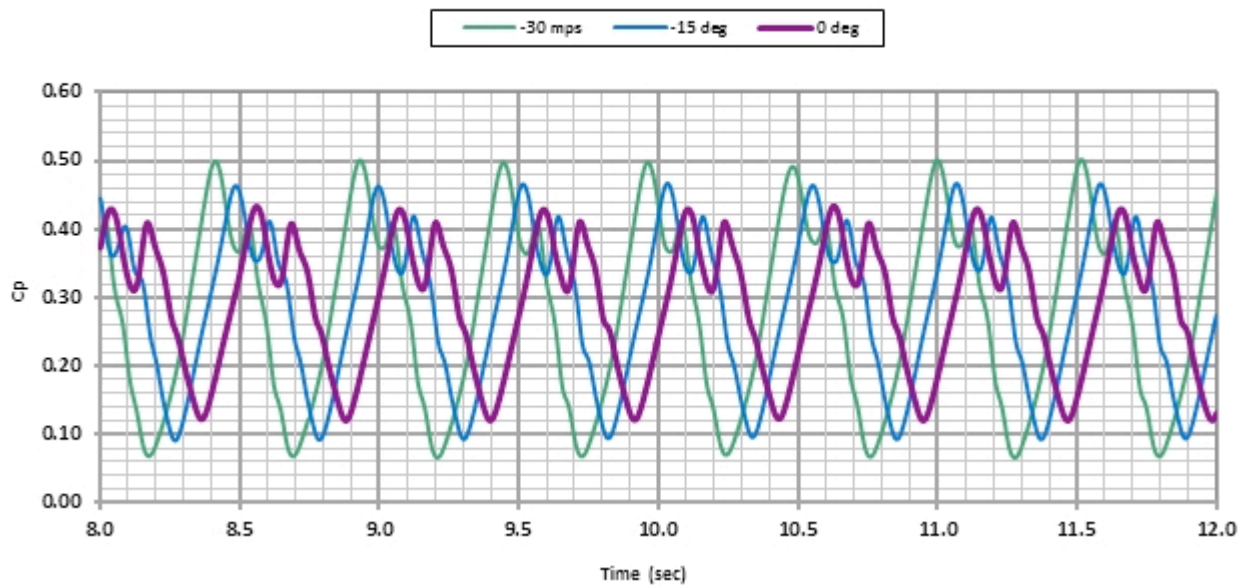


Figure 48: Plot of power coefficient for north-westerly wind directions (Wind speed = 18.1301 m/s, $TSR = 2$).

Table 12: Torque and power coefficient predictions for the WHI 3000 model for different wind directions using CFD

TSR	Wind Speed		γ (deg)	C_m	C_P	% C_{P0}
2.00	18.13	m/s	-30.00	42.494	0.283	-2.211
	40.56	mph	-15.00	43.808	0.292	0.814
			0.00	43.454	0.290	--
			15.00	42.285	0.282	-2.691
			30.00	40.958	0.273	-5.744

9. SPACING STUDY FOR MULTIPLE WHI 3000 TURBINES (TASK 3.5)

9.1 Problem Description

CFD is used to study the vortex effect sensitivity to the distance between the turbines. The flow over three WHI 3000 turbines placed in a linear array as shown in Figure 49 is simulated. The top rotor is rotating counter clockwise, the middle rotor is rotating clockwise and the bottom rotor is rotating counter clockwise. The flow conditions are set: the angular velocity of all turbines is $\omega = 29$ rpm, the wind velocity of almost $V = 18$ m/s for TSR = 2 and Reynolds number is around 2 million. The large Reynolds number ensures that the problem is in turbulent regime and the turbulence model selected is appropriate.

The distance between 2 rotors is defined as H . It measures the distance between the circular blades path. This distance is varied and the C_P is calculated in each case. The H value of 1.91 m is the baseline, which corresponds to a distance between rotors axis of 1.08 rotor diameters.

This report only presents simulations at TSR = 2 and TSR = 3. The parameters for calculations used are similar to other studies.

Table 13 summarizes these parameters. Three calculations are performed with 3 different values of the spacing: $H = 0.75H^0$, $H = H^0$ and $H = 3H^0$. The results for a single rotor with a time step of 0.003 and second order simulations are also reported in the table.

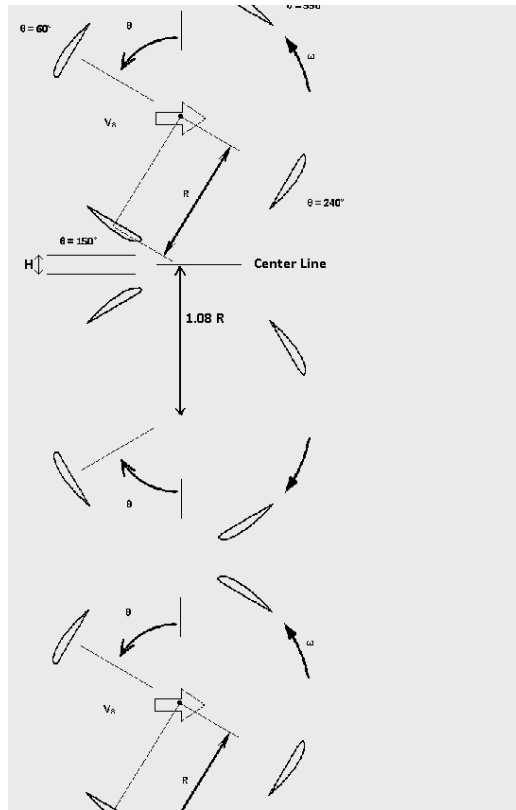


Figure 49: Schematic of an array of 3 WHI 3000 turbines indicating the spacing H.

Table 13: Parameters used for the flow calculations

Version	Double precision	
Viscous Model	Spalart-Allmaras (1 equation)	
Solver	Unsteady 2 nd order implicit	
Number of elements	(2.87M)(2.87M) (3.29M)	
Number of nodes	(2.89M)(2.89M)(3.30M)	
Convergence criteria	Continuity	1e-8
	x-velocity	1e-6
	y-velocity	1e-6
	Nut	1e-6
Time step size	0.003	
Number of processors used to run the simulation	8	

9.2 Analysis at TSR = 2

Figure 50 shows the C_P values as the simulation is converged in time. Convergence is obtained once the C_P obtained has a periodic behavior. As seen in the figure, all 3 curves reach the same oscillatory behavior. The average C_P is calculated over the last full rotation.

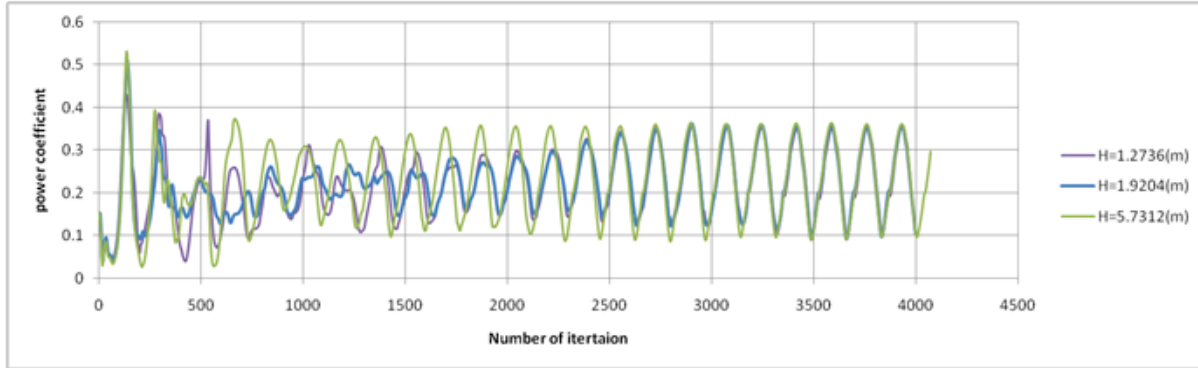


Figure 50: Variation of power coefficient vs. iterations.

The instantaneous velocity flow field is shown in Figure 51. Wakes and vortex shedding are visible in the dark blue coloring. The streamlines for 2 of the airfoils in the first and fourth quadrant are reported in Figure 52. Note that the azimuthal angle for the middle rotor is defined clockwise as illustrated in Figure 53.

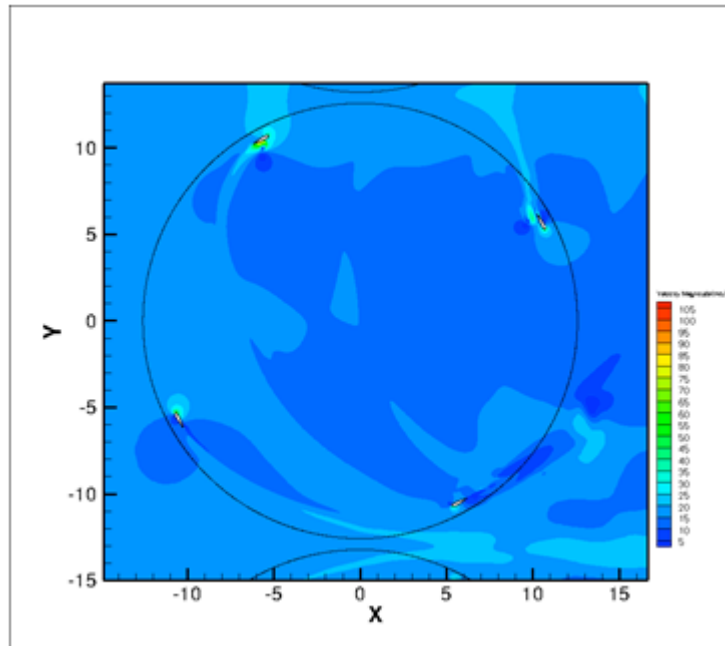


Figure 51: Velocity magnitude (m/s) of the middle rotor.

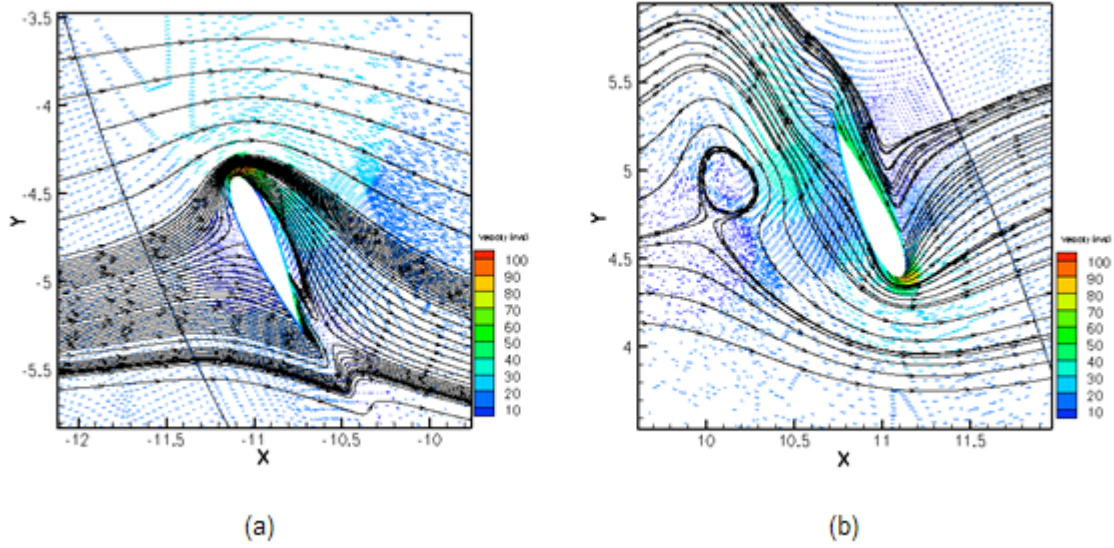


Figure 52: Streamlines around the blades in the first quadrant (a) and in the fourth quadrant (b).

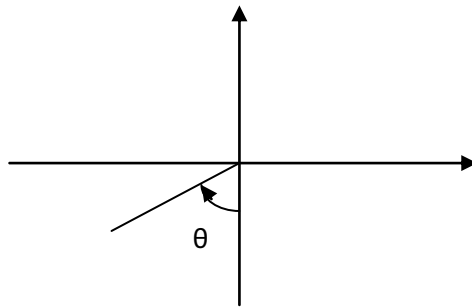


Figure 53: Definition of the azimuthal angle for the middle rotor.

Table 14 presents the mesh size used for each calculation, the number of iterations and the CFD calculated value of the C_p . We note that all the values of the C_p are very close for the 3 difference spacing of the rotor. These values are nevertheless smaller than the 1 rotor ($C_p = 0.26$). This will be discussed in the following section.

Table 14: Summary of simulations and C_p values

Run	Gap Size (m)	Number of Elements	Number of Nodes	Number of Iterations	C_p
0	Single Rotor	1,193,618	1,198,546	4000	0.261
1	1.2736	2,876,824	2,891,051	4000	0.236
2	1.9102	2,872,634	2,886,861	4000	0.237
3	5.7312	3,290,382	3,304,609	4000	0.238

Though the values of the C_P are similar the torque on the blades during a full rotation are different. For the spacing H^0 and $3H^0$ identical curves are observed while the torque curve for the spacing $0.75 H^0$ is different in the last quadrant. This difference does not affect the overall C_P , but does indicate an effect of the proximity of the blades.

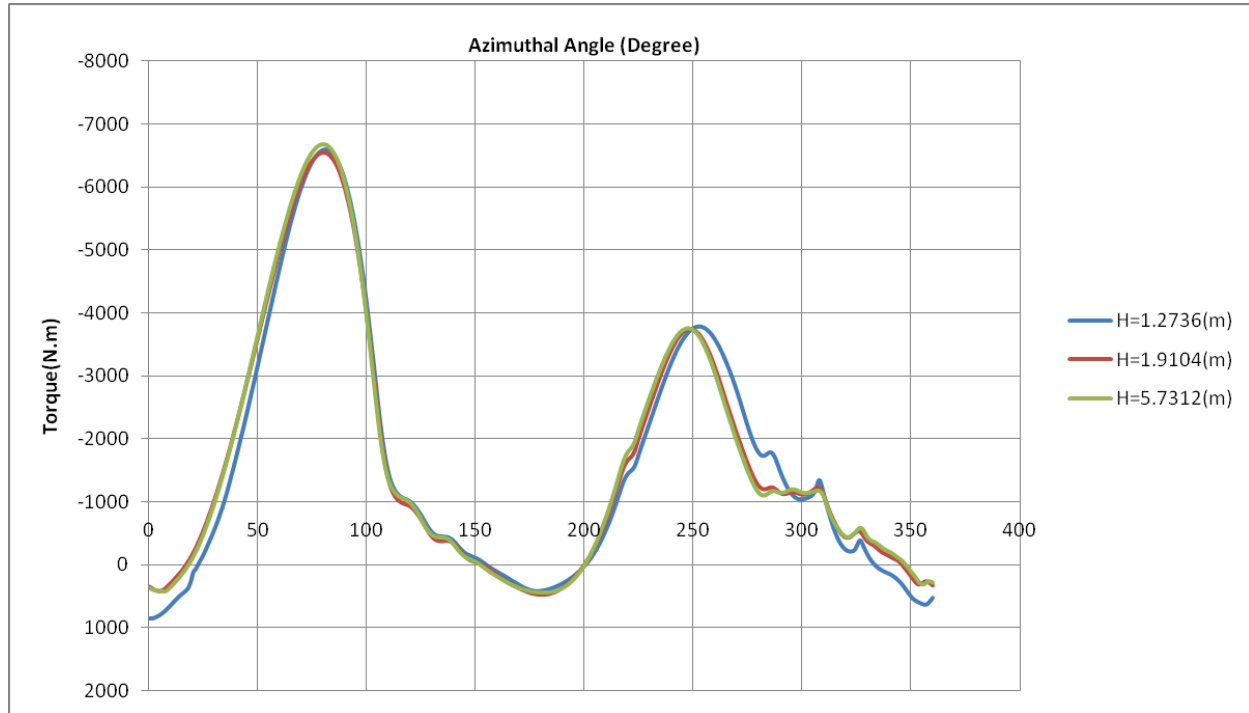


Figure 54: Variation of Torque (Nm) of the blade vs. azimuthal angle.

9.3 Analysis of Different Rotation Speed of the Top and Bottom Rotors

In an attempt to understand the decrease of C_P at $TSR = 2$ between 1 and 3 rotors, a simulation with the top and bottom rotors at a slower speed was performed. The rotation speed was reduced to 5 rpm for the top and bottom rotor, but was maintained to the middle rotor to the original 29 rpm. The distance between the turbines was kept as the original H distance. The C_P calculation for the middle rotor gave a value of 0.257. This indicates that at $TSR = 2$, the vortex effect is very weak and the blockage effect does not reduce the C_P . Note that this conclusion is restricted to this large turbine type (WHI 3000) and for $TSR = 2$. From Figure 55, we see that the main difference between the curves is in the last quadrant, when the blades from the middle rotor and the bottom rotor get closer to each other.

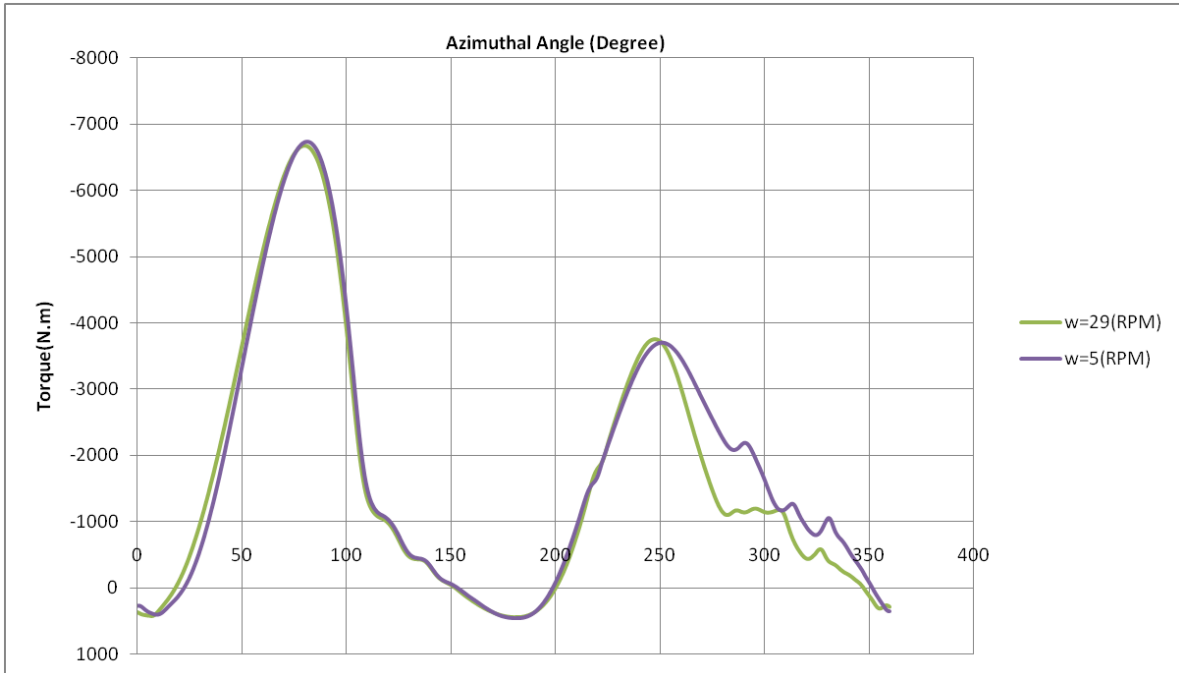


Figure 55: Variation of Torque (Nm) of the blade vs. azimuthal angle for turbines with different rotating speeds.

9.4 Analysis for TSR = 3

For TSR = 3, simulations for 1 and 3 original distances between rotors indicate the same C_p of 0.49. For 1 rotor, the C_p is 0.43. Clearly, in this case the vortex effect is stronger as seen in Figure 56.

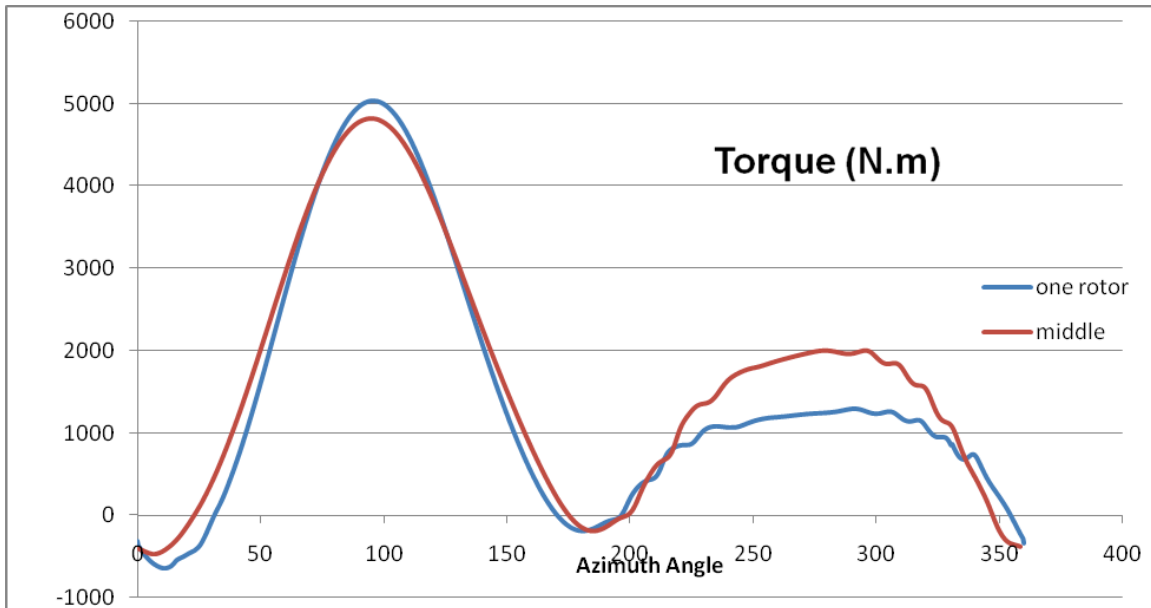


Figure 56: Variation of Torque (Nm) of the blade vs. azimuthal angle for TSR = 3.

To understand the difference between the TSR = 2 and TSR = 3, we plot the moment coefficient as defined below:

$$C_m = \frac{M}{0.5 \cdot \rho \cdot V_\infty^2 \cdot A \cdot l} \quad (10)$$

M: Moment
 ρ : Density
 V_∞ : Free stream velocity
 $A = D$: Front Area
 $l = R$: Rotor Radius

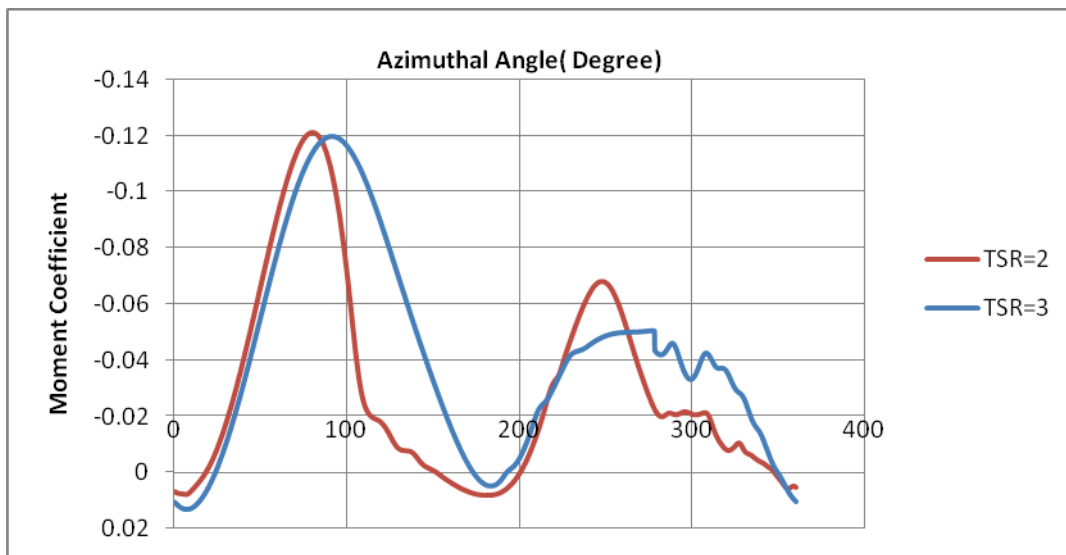


Figure 57: Moment coefficient vs. azimuthal angle for TSR = 2 and TSR = 3.

Figure 57 shows that for TSR = 3, the curve is wider in the region where the blades get closer to the neighboring rotor, i.e. in the second and fourth quadrants. Note that at TSR = 3, the maximum angle of attack of the blades is smaller. This may indicate why the curve for TSR = 2 falls rapidly at around the angle of 100 degrees.

10. TORQUE LIMITING PITCH ANALYSIS (TASKS 4.1, 4.2 AND 4.3)

10.1 Objectives

In order to limit the WHI 3000 model wind turbine generator power to below 75 kW, the following objectives of the torque limiting analyses were specified by WHI:

- a. Only 2 of the 4 blades of the Model 3000 will pitch leading edge towards the center of the rotor.
- b. Pitching is initiated prior to maximum generator power of 75 kW.
- c. Pitch angles of the 2 diametrically opposed blades will be equal.
- d. The blade pitch mechanism is damped and is expected to respond to average rather than instantaneous torque.
- e. Pitch angles should be function of the wind speed and not rotor azimuthal angle.
- f. The TSR range analyzed is low enough to be within the CARDAAV analytical range.
- g. Blade lift, drag, pitching moment and center of pressure data required at wind speed increments of 2 mph starting when generator power reaches 74 kW and extended up to a wind speed of 60 mph.

With the above objectives at hand, the following methodology was adopted to accomplish the torque limiting analyses.

10.2 Methodology

The CARDAAV code was setup to allow 2 out of the 4 WHI 3000 turbine diametrically opposed blades to pitch. The pitch was specified as input. The resulting torque and power were then based on the average of the torque and power of the individual blades, respectively. Analysis were then carried out at wind speed increments of 2 mph starting from a wind speed of 24 mph, when generator power just exceeds 75 kW, to 60 mph. Since the output torque and power are directly related, in the analysis the turbine power is used as a constraint rather than the torque at 75 kW power rating. The blade pitch variable was interactively varied to limit the power below 75 kW at each wind speed. The results of the analyses are provided in the next section and also detailed in the accompanying MS Excel file.

10.3 Torque Limiting Pitch Results

Figure 58 shows a comparison of the output power for the WHI 3000 wind turbine with and without the torque limiting blade pitch. The blade pitch used to limit the power to below 75 kW is shown in Figure 59. A summary of the results for wind speed increments of 2 mph is listed in Table 15. Please note that the variables P_{wo} and P_{wp} in Table 15 stand for power without and with pitched blades, respectively. As one would expect intuitively, an increased pitch is required at higher wind speeds to limit the power and hence the turbine torque. The results indicate that the blade pitch must vary from 6.5 degrees at 24 mph to 14 degrees at 60 mph to keep maximum power output below 75 kW.

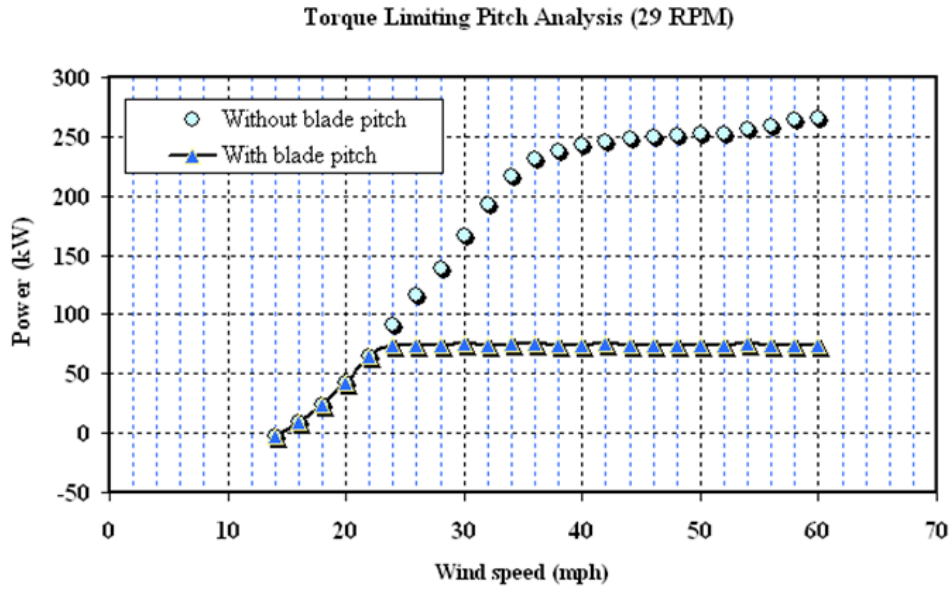


Figure 58: Plot of the power curve for the WHI 3000 wind turbine with and without the torque limiting blade pitch at 2 mph increments.

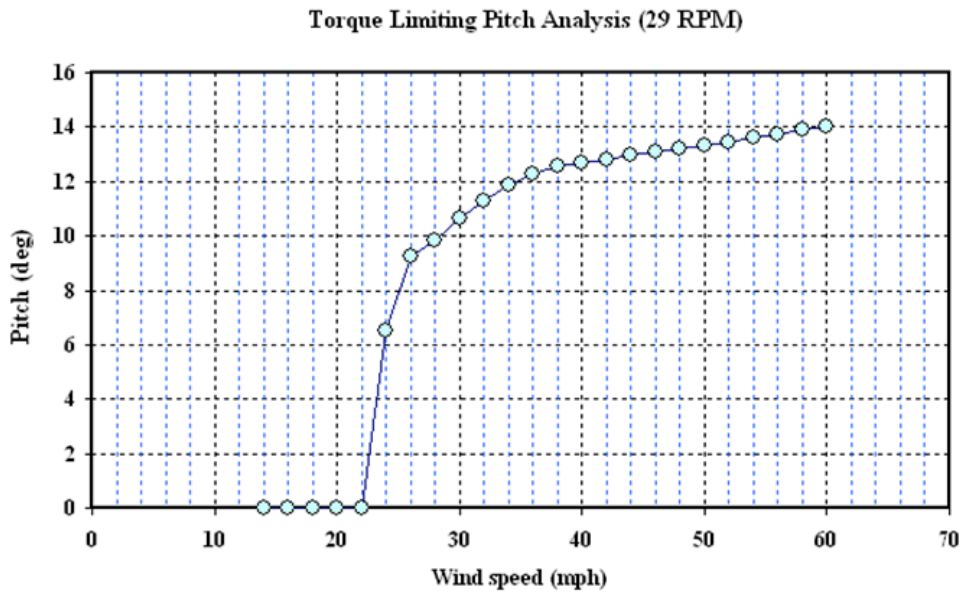


Figure 59: Plot of the WHI 3000 wind turbine torque limiting blade pitch vs. the wind speed at 2 mph increments.

Table 15: Results of the torque limiting pitch analyses at 2 mph increments

Wind speed		P_{wo}	Pitch	P_{wp}
mph	m/s	kW	deg.	kW
14	6.26	-2.63	0.00	-2.63
16	7.15	9.41	0.00	9.41
18	8.05	24.19	0.00	24.19
20	8.94	42.39	0.00	42.39
22	9.84	64.44	0.00	64.44
24	10.73	91.0	6.50	74.47
26	11.62	116.0	9.25	74.79
28	12.52	139.0	9.85	74.80
30	13.41	167.0	10.65	74.85
32	14.31	193.0	11.30	74.74
34	15.20	217.0	11.85	74.94
36	16.09	231.0	12.25	74.82
38	16.99	238.0	12.55	73.97
40	17.88	243.0	12.70	74.72
42	18.78	246.0	12.80	74.91
44	19.67	248.0	12.95	74.31
46	20.56	250.0	13.10	74.31
48	21.46	251.0	13.20	74.74
50	22.35	252.0	13.35	74.59
52	23.25	253.0	13.45	74.75
54	24.14	257.0	13.60	74.94
56	25.03	259.0	13.75	74.08
58	25.93	265.0	13.90	74.80
60	26.82	266.0	14.00	74.30

V = 60 mph / 26.822 m/s													Blades with pitch = 14 deg		
Blades without pitch													Blades with pitch = 14 deg		
Azimuth	Re	Alpha	Cl	Cd	Cmc1	Cmc2	Lift N	Drag N	M_c1 N-m	M_c2 N-m	Re	Alpha	Cl		
-87.5	4097155	1.049	0.11458	0.00743	0.00126	0.02990	1063.81	68.98	11.36	270.67	4186276	-12.920	-1.20989		
-82.5	4089557	3.147	0.34366	0.00816	0.00351	0.08943	3190.70	75.76	31.81	809.54	4178455	-10.760	-0.96734		
-77.5	4074377	5.242	0.57244	0.00763	0.00502	0.14813	5314.80	70.84	45.47	1340.95	4162828	-8.603	-0.84528		
-72.5	4012631	7.234	0.78971	0.00743	0.00534	0.20276	7332.04	68.98	48.31	1835.50	4118302	-6.500	-0.67497		
-67.5	3982807	9.291	1.01415	0.00757	0.00412	0.25765	9415.84	70.28	37.26	2332.37	4087385	-4.365	-0.46889		

Figure 60: Header of a typical wind speed worksheet.

71	242.5	3801678	-10.711	-0.97163	0.01768	-0.00217	-0.24508	-9021.07	164.15	-19.64	-2218.53		3864381	-24.991	-0.89530
72	247.5	3836807	-8.779	-0.85289	0.01548	-0.00459	-0.21781	-7918.63	143.72	-41.52	-1971.69		3900417	-23.007	-1.00566
73	252.5	3865002	-6.837	-0.70292	0.01302	-0.00538	-0.18111	-6526.24	120.88	-48.71	-1639.48		3929338	-21.014	-1.07099
74	257.5	3994403	-5.096	-0.54151	0.01084	-0.00495	-0.14033	-5027.63	100.64	-44.82	-1270.31		3869403	-18.855	-1.02957
75	262.5	4009161	-3.059	-0.33398	0.00940	-0.00343	-0.08693	-3100.83	87.27	-31.06	-786.88		3883467	-16.915	-1.02435
76	267.5	4016548	-1.020	-0.11136	0.00833	-0.00122	-0.02906	-1033.92	77.34	-11.05	-263.07		3890506	-14.972	-1.01954
77															
78	Stats	Re	Alpha deg	Cl	Cd	Cm_{c/4}	Cm_{c/2}	Lift N	Drag N	M_{c/4} N.m	M_{c/2} N.m		Re	Alpha deg	Cl
79															
80	Min	612562	-44.843	-3.23462	0.00743	-0.19519	-0.64104	-30031.73	68.98	-1766.91	-5802.92		620473	-58.772	-4.63401
81	Max	4097155	46.796	1.82480	1.22773	0.19570	0.41961	16942.30	11398.82	1771.53	3798.45		4186276	32.666	1.89947
82	Mean	2628232	0.949	0.03785	0.48990	-0.00110	0.00836	351.42	4548.44	-9.99	75.67		2648489	-12.988	-0.17961
83															

Figure 61: Footer of a typical wind speed worksheet.

Detailed results of the blade lift, drag and pitching moment are provided in the accompanying MS Excel file titled “Torque-limiting-analyses-data.xls.” A snap shot of the header and footer from the Excel data file is provided in Figures 60 and 61, respectively. The results for each wind speed are appended in separate worksheets with the wind speed value as the worksheet tab label (see Figure 61). Separate data for the case without and with blade pitch are listed in each worksheet. These are listed under the headings “Blades without pitch” and “Blades with pitch = xx deg” (see Figure 60). A brief explanation of the data under these headings in each column is as follows:

- Column A: Azimuth angle in 5 degrees increments starting from the upwind half of the rotor.
- Columns B & M: Blade Reynolds number based on rotational speed and blade radius.
- Columns C & N: Blade effective angle of attack α_{eff} (= Incidence angle α – Pitch angle α_0) in degrees.
- Columns D & O: Blade lift coefficient (C_l) based on effective angle of attack (experimental data).
- Columns E & P: Blade drag coefficient (C_d) based on effective angle of attack (experimental data).
- Columns F & Q: Blade quarter-chord moment coefficient ($C_{m_{c/4}}$) based on effective angle of attack (empirical data).
- Columns G & R: Blade mid-chord moment coefficient ($C_{m_{c/2}}$) based on effective angle of attack (empirical data).
- Columns H & S: Blade lift ($L = \frac{1}{2}\rho(R\omega)^2cbC_l$) in Newton.
- Columns I & T: Blade drag ($D = \frac{1}{2}\rho(R\omega)^2cbC_d$) in Newton.
- Columns J & U: Blade moment at quarter-chord location ($M_{c/4} = \frac{1}{2}\rho(R\omega c)^2bC_{m_{c/4}}$) in Nm.
- Columns K & V: Blade moment at mid-chord ($M_{c/2} = \frac{1}{2}\rho(R\omega c)^2bC_{m_{c/2}}$) in Nm.

Here, columns B through K list data for the wind speed case without blade pitch, while columns M through V list data for the case with blade pitch. The footer of each wind speed worksheet provides some basic, but valuable statistics for each column (see Figure 61). These statistics include the minimum (Min), maximum (Max) and the average (Mean) values for each of the data columns.

An explanation of the 2 different moment coefficients provided can be best depicted with the illustration provided in Figure 62. In this figure, the different force (lift, drag) and moment coefficients are shown. Since the blade profile uses a symmetric NACA0018 airfoil section, the airfoil center of pressure coincides with its aerodynamic center which is typically very close to the quarter-chord ($c/4$) location. Typical moment coefficient data found in literature is usually referenced to the quarter-chord ($c/4$) location. Since in the WHI 3000 turbine, the blade attachment point is at mid-chord ($c/2$) location, the mid-chord moment coefficient can be calculated through the transformation of the forces and moment about the mid-chord ($c/2$) location. This simple transformation is given by the following relation in non-dimensional form:

$$C_{m_{c2}} = C_{m_{c4}} + (\frac{1}{2} - \frac{1}{4}) C_l = C_{m_{c4}} + \frac{1}{4} C_l \quad (11)$$

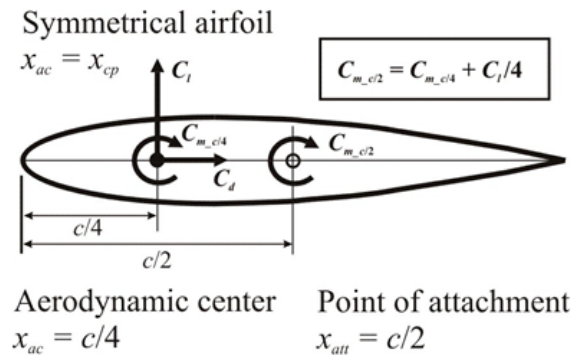


Figure 62: Symmetrical airfoil lift, drag and moment coefficients.

The NACA0018 airfoil data was obtained through an approximation of the available quarter-chord moment coefficient data [13, 14]. The approximation was necessary because of the large scatter found in the wind tunnel data [13] as shown in Figure 63. In the figure, WAT refers to Ref. [13], whereas AHR refers to Ref. [14]. The experimental data of Ref. [13] also shows a hysteresis effect which is difficult to simulate numerically. Thus, an approximation of the data was used to empirically obtain the quarter-chord moment coefficient data using a combination of experimental and analytical data [14, 15]. The approximation is shown as red circles in Figure 63. A curve-fit was obtained using a trend line. The equation of the trend line is:

$$C_{m_{c4}} = 3.3248 \times 10^{-9} \alpha_{eff}^5 - 9.13371223 \times 10^{-7} \alpha_{eff}^3 + 1.20663679416 \times 10^{-3} \alpha_{eff} \quad (12)$$

The above relation was used in the analyses to calculate the quarter-chord moment coefficient based on the effective angle of attack α_{eff} .

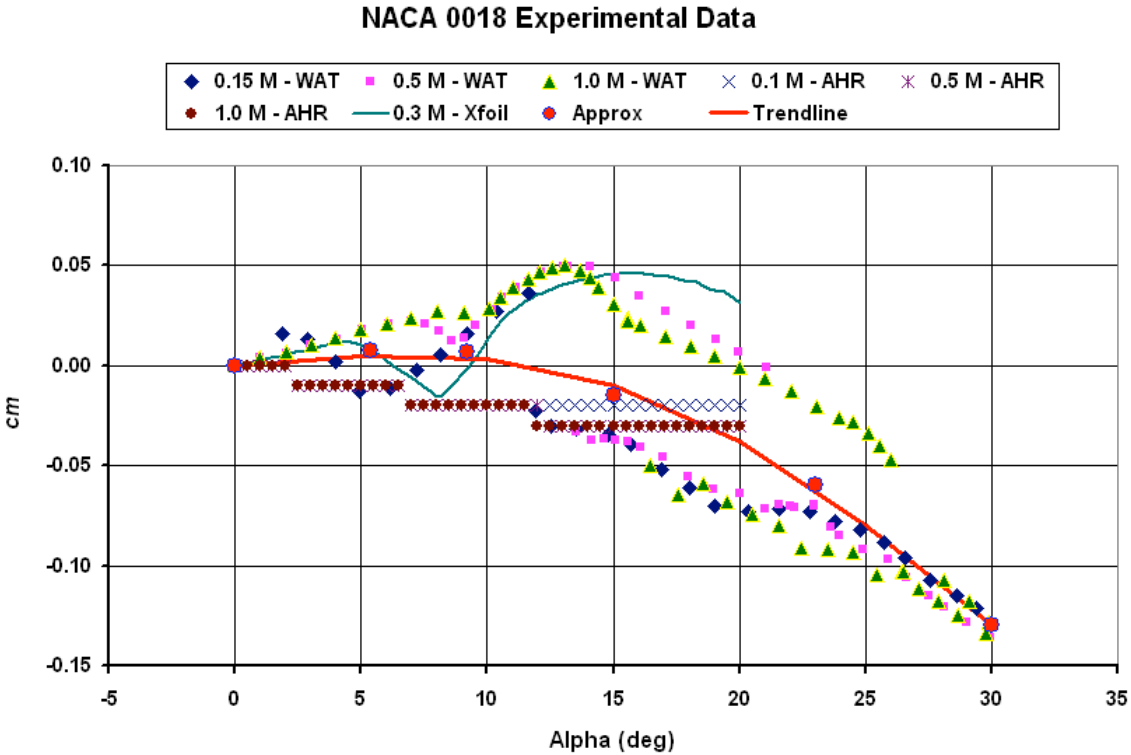


Figure 63: NACA0018 airfoil quarter-chord moment coefficient data: experiments vs. theoretical.

11. CONCLUSIONS AND RECOMMENDATIONS

This project, carried out by IOPARA Inc. as a contract project for Wind Harvest International Inc. was completed successfully and the experience gained by IOPARA Inc. in the specific nature of the unique simulations was invaluable.

As part of this project, the CARDAAV code was implemented in order to perform the variable pitch optimization and the requested data are provided in the MS Excel file attached to this report.

Among the different rotor solidities analyzed as part of the solidity parametric study, a rotor solidity of 16.5 % would provide the highest power coefficient ($C_p = 49.38\%$ at $TSR = 3.01$, with coupled vortex effect). One should also mention that the performances of the different rotor solidities of the WHI 3000 were calculated using the same interference factors, calibrated for the rotor solidity of 16.5 %. Calibration of the interference factors for the other rotor solidities would require additional CFD simulations.

Concerning the drag evaluation, the analysis showed similar trends for the WHI 1500 and extended WHI 1500 (WHI 3000), the main difference in the results between the two rotors was the smaller parasitic drag values for the WHI 1500 due to the shorter struts. The results also showed that NACA0030 shaped fairings would offer the lowest parasitic drag among the different cross-sections analyzed. If a lenticular cross-section is to be used (e.g. for economic reasons), a t/c ratio of 18 % would be suggested. Moreover, the results showed that for lenticular cross-sections of similar t/c ratios, moving the maximum thickness from $c/2$ to $c/3$ would be preferable. In addition, modifying the end of the blade arm geometry to act as properly sized endplate would further increase the power produced by the turbine, especially for the WHI 3000 model.

From the column placement analysis, it appears that there is no significant change in the power coefficient for the cases with or without columns. This conclusion is based on the calculation of the power coefficient for 2 different TSR and by analyzing the torque for 1 blade in each configuration. This work was done for the WHI 3000 turbine, but the conclusions reached should also be applicable for the WHI 1500 turbine.

The effect of wind direction was also investigated for a 3-rotor configuration. The results presented predict that north-westerly wind directions can result in a slight increase in the power coefficient for both the co-rotating and counter-rotating rotor configurations. This increase is more in case of the co-rotating rotors. The power coefficient C_p history (time) plots show that south-westerly wind directions introduces a lag in C_p values, while north-westerly directions show an opposite trend. The results suggests that the turbine could be sited to take advantage of the northerly wind (with reference to the 3-rotor turbine axis) and thus, preserve the omni-direction advantage of vertical axis wind turbines in an overall sense.

Finally, the CFD simulations of different turbines spacing was able to identify some particular behavior of the WHI 3000. The distance between rotors up to $3H$ has no influence on the C_p . At $TSR = 2$ the vortex effect is very weak. The blockage effect of the bottom rotor is dominant and reduced the C_p . It may be beneficial to have only pairs of rotors but this has not been investigated. At $TSR = 3$ the vortex effect is strong.

APPENDIX 1

As seen in Figure 64, in the given Re range, the S-A model overestimate the C_d by 40 % in average due to disregarding laminar flows in the boundary layer. With a 40 % correction factor applied on all values, we get a nearly perfect match between experimental and simulated data as seen in Figure 65 and Table 16. The same correction factor was applied to all computed C_d values of section 5.

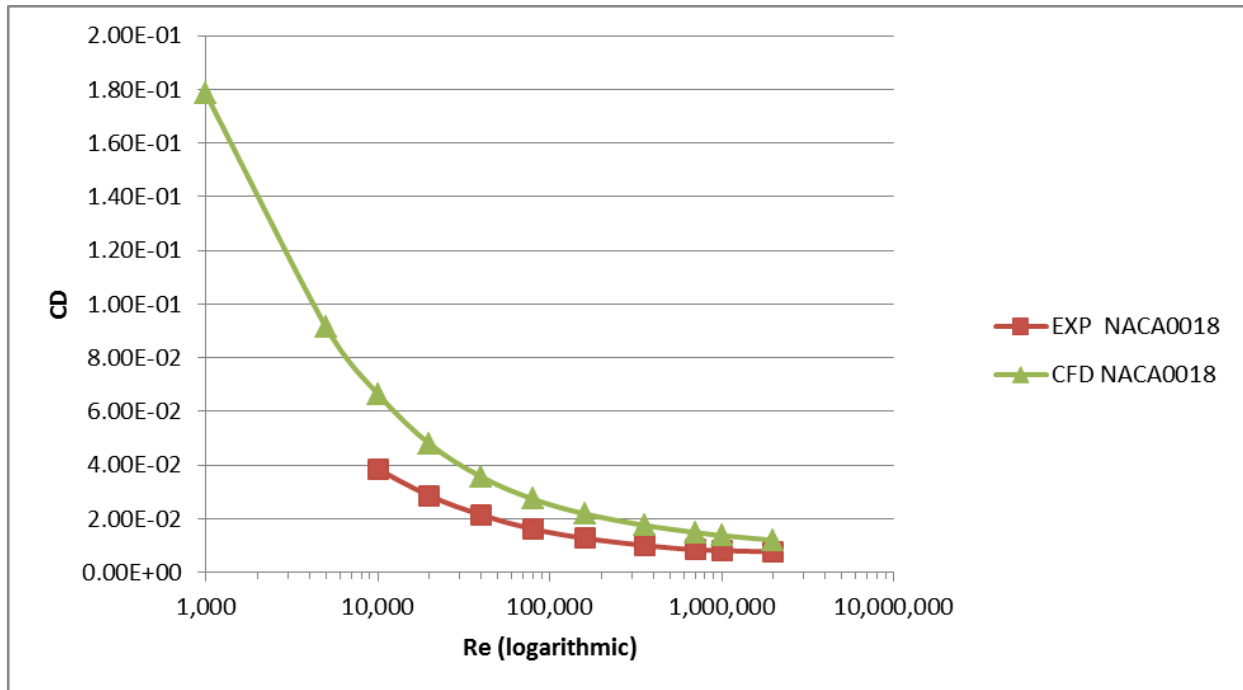


Figure 64: NACA0018 drag coefficient (C_d) Vs. Reynolds number (Re) (logarithmic scale), for experimental and simulated values.

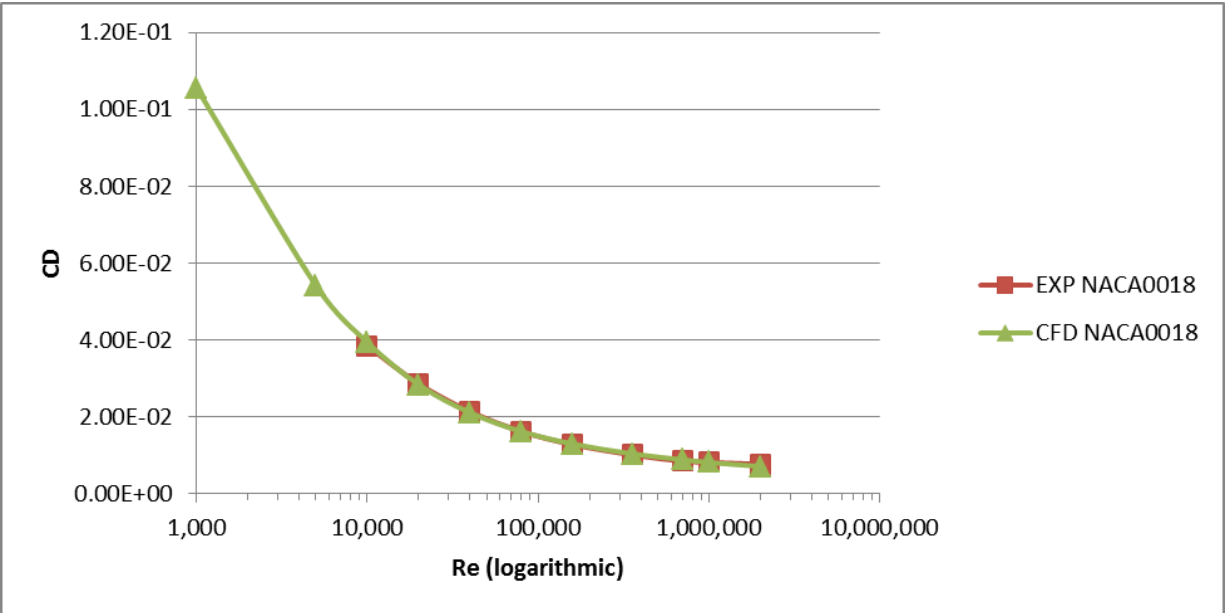


Figure 65: NACA0018 drag coefficient (C_d) Vs. Reynolds number (Re) (logarithmic scale), for experimental and simulated values with correction factor.

Table 16: Compared values between experimental data an CFD generated data with 40 % correction factor

Re	Experimental	CFD
1,000		1.06E-01
5,000		5.42E-02
10,000	3.85E-02	3.94E-02
20,000	2.86E-02	2.84E-02
40,000	2.14E-02	2.11E-02
80,000	1.62E-02	1.62E-02
160,000	1.28E-02	1.30E-02
360,000	1.01E-02	1.04E-02
700,000	8.50E-03	8.87E-03
1,000,000	8.20E-03	8.19E-03
2,000,000	7.70E-03	7.12E-03

REFERENCES

1. I. Paraschivoiu, *Wind Turbine Design with Emphasis on Darrieus Concept*, Polytechnic International Press, Montreal, 2002.
2. I. Paraschivoiu, O. Trifu and F. Saeed, "H-Darrieus Wind Turbine with Blade Pitch Control," *International Journal of Rotating Machinery*, vol. 2009, Web Article ID 505343, Aug. 2009.
3. I. Paraschivoiu, F. Saeed and V. Desobry, "New Algorithms for Wind Turbine Performance Prediction and Optimal Design," *International Symposium on Transport Phenomena*, Victoria, British Columbia, 2009.
4. H. Widell, "Genial 1.1, a Friendly Function Optimizer based on Evolutionary Algorithms", Available: <http://www.hjem.get2net.dk/widell/>.
5. Y. Staelens, F. Saeed and I. Paraschivoiu, "A Straight-Bladed Variable-Pitch VAWT Concept For Improved Power Generation," *22nd ASME Wind Energy Symposium held in conjunction with the 41st Aerospace Sciences Meeting & Exhibit*, Reno, NV, US, 2003.
6. V. Desobry, "Aerodynamic Performance of Darrieus Vertical Axis Wind Turbines," Final Report, Mechanical Engineering Department, École Polytechnique de Montréal, August 2002.
7. IOPARA Inc., "Aerodynamic Model of the Wind Harvest International 3000 Wind Turbine," Final report prepared for Wind Harvest International Inc., November 2009.
8. IOPARA Inc., "Aerodynamic Model of the Wind Harvest International Model 1500 Wind Turbine," Final report prepared for Wind Harvest International Inc., May 2009.
9. M. L. Ray, A. L. Rogers and J. G. McGowan, "Analysis of wind shear models and trends in different terrains," *AWEA Windpower 2005 Conference*, Pittsburgh, PA, 2006.
10. R. E. Sheldahl and P. C. Klimas, "Aerodynamic Characteristics of Seven Airfoil Sections Through 180 Degrees Angle of Attack for Use in Aerodynamic Analysis of Vertical Axis Wind Turbines," Tech. Rep. SAND80-2114, Sandia National Laboratories, Albuquerque, New Mexico, March 1981.
11. S. F. Hoerner, "Fluid-dynamic drag: practical information on aero-dynamic drag and hydrodynamic resistance," in *Hoerner Fluid Dynamics*, Brick Town, N. J., 1906.
12. M. Paraschivoiu, C. X. Zhang, S. Jeyatharsana, N. V. Dy, F. Saeed, R. N. Thomas and I. Paraschivoiu, "CFD Analysis of Vertical Axis Wind Turbines in Close Proximity," submitted to *Wind Energy*.

13. W. A. Timmer, “Two-Dimensional Low-Reynolds Number Wind Tunnel Results For Airfoil NACA 0018,” *Wind Engineering*, vol. 32, no. 6, pp. 525–537, 2008.
14. I. Skias, *Airfoil and Hydrofoil Reference* [Software], SKIAS Engineering, 2007.
15. M. Drela, “XFOIL: An Analysis and Design System for Low Reynolds Number Airfoils,” *Lecture Notes in Engineering: Low Reynolds Number Aerodynamics*, T. J. Mueller (ed.), vol. 54, Springer-Verlag, New York, pp. 1–12, 1989.